• U C •

FCTUC FACULDADE DE CIÊNCIAS
E TECNOLOGIA
UNIVERSIDADE DE COIMBRA

DEPARTAMENTO DE
ENGENHARIA MECÂNICA

Numerical Modelling of Contact between Rough Surfaces

Submitted in Partial Fulfilment of the Requirements for the Degree of Master in Mechanical Engineering in the speciality of Production and Project

Modelação Numérica do Contacto entre Superfícies Rugosas

Author

Mariana Filipa Simões Moura

Advisor

Diogo Mariano Simões Neto

Jury

President	**Professor Doutor Pedro André Dias Prates** **Professor Convidado da Universidade de Coimbra**
Vowel	**Professor Doutora Marta Cristina Cardoso de Oliveira** **Professor Auxiliar da Universidade de Coimbra**
Advisor	**Professor Doutor Diogo Mariano Simões Neto** **Professor Convidado da Universidade de Coimbra**

Coimbra, February, 2017

“Yesterday is history, tomorrow is a mystery, but today is a gift. That is why it is called the present.”

Unknown

ACKNOWLEDGEMENTS

This work and my degree in engineering would not be possible without the help and support of my family and friends as well as the guidance of the teachers through this educational path.

First and foremost I'm particularly grateful to my scientific advisor Professor Diogo Mariano Simões Neto for the dedication during this work. From the constructive suggestions, through the transmitted knowledge to the willingness to give his time and answer all my questions and doubts, it has been a privilege, thank you. I'm also grateful for the advice given by Professor Marta Cristina Cardoso de Oliveira as well as the assistance from Professor Pedro André Dias Prates, it was a great help to overcome the difficulties that have arisen.

Secondly, I want to thank especially my good friend Nicolas Marques for all the time and suggestions, he was always available and helpful. Thank you for the encouragement and friendship.

I want to thank my friends and colleagues from all these years. António Camilo and André Brás, thank you for all the help and fellowship, as well as Hugo Matos, Vânia Sousa, Diana Almeida, André Travassos, Ana Frias thank you for all the good memories.

Finally, I want to thank my family for their unconditional love and support, namely my parents, without whom none of this would be possible.

This work was carried out under the project "Improving the manufacturing of metallic bipolar plates for fuel cells using the rubber forming process" with reference P2020-PTDC/EMS-TEC/0702/2014, co-funded by the Foundation for Science and Technology and the EU/FEDER, through the program COMPETE 2020 with reference POCI-01-0145-FEDER-016779.

Abstract

The effectiveness of sheet metal forming simulation is strongly affected by the accuracy of the friction model used. Studies about the cause and mitigation of friction have been developed over the last two millennia. Despite all the information reported, numerical simulation still relies on Coulomb' law, which considers only a single parameter obtained by experimental tests.

The main objective of this work is to study numerically the contact between rough surfaces. In order to develop this study, two- and three-dimension finite element models of an asperity were created and the simulations were carried out by the in-house finite element code DD3IMP. Several materials are compared by changing the mechanical material parameters (Young's modulus, yield stress and Poisson's ratio) and different geometrical parameters (height of the asperity's tip) are studied. This allows covering a wide range of contact situations, highlighting the role of each parameter on the asperity deformation.

In both models studied, for an asperity with the highest tip, the material reaches the yield inception at a lower interference and, consequently, the contact area is smaller. Based on the load parameter α and the plasticity index ψ, it is possible to predict the actual material regime (elastic or plastic). Regarding the 3D model, with the exception of Poisson's ratio, all the material parameters considered greatly influence the value of contact radius to the plastic regime. The ratio between the effective contact area and the apparent contact area, which is very low, presents a linear increase as a function of the real contact area. Besides, this ratio is higher when predicted with the 2D model than in the 3D model.

Keywords: Surface Roughness, Finite Element Analysis, Plastic Inception, Frictionless Contact, Sinusoidal Profile, Elastic-Plastic deformation.

Resumo

A eficácia da simulação numérica de um processo de estampagem está intrinsecamente ligada ao modo como o contacto com atrito é modelado. Nos últimos dois milénios, têm sido desenvolvidos muitos estudos para perceber as causas do aparecimento de atrito e como o reduzir. No entanto, a simulação numérica ainda recorre à lei de Coulomb, expressando as forças de atrito apenas por um parâmetro obtido experimentalmente.

O principal objectivo deste trabalho é estudar numericamente o contacto entre superfícies rugosas. Para concretizar esta análise, construíram-se dois modelos de elementos finitos de uma asperidade, um em duas dimensões e outro em três dimensões, sendo as simulações realizadas com recurso ao programa académico de elementos finitos DD3IMP. Vários materiais foram testados, comparando a influência dos vários parâmetros (módulo de Young, tensão de cedência e coeficiente de Poisson) assim como a geometria (altura) da asperidade. Este procedimento permite estudar uma vasta gama de situações de contacto e perceber qual a importância de cada parâmetro na deformação da asperidade.

Em ambos os modelos estudados verificou-se que a transição do regime elástico para o regime plástico ocorre mais cedo quando a ponta da asperidade é mais alta, resultando numa área de contacto menor. Com base no parâmetro de carga α e no índice de plasticidade ψ, é possível prever o regime do material (elástico ou plástico). Em relação ao modelo 3D, à excepção do coeficiente de Poisson, todos os parâmetros do material apresentam uma forte influência no raio de contacto aquando da transição para o regime plástico. A razão entre a área de contacto real e a aparente revela-se bastante pequena e pode ser descrita por uma função linear quando representada em função da área real de contacto. Para além disso, o rácio é mais elevado quando é obtido usando o modelo 2D.

Palavras-chave: Rugosidade Superficial, Análise de Elementos Finitos, Inicio da Plastificação, Contacto sem Atrito, Perfil Sinusoidal, Deformação Elástico-Plástica.

Table of Contents

LIST OF FIGURES

LIST OF TABLES

SYMBOLS AND ACRONYMS

Variables and Symbols

a – Contact Radius

A_r - Contact Area

A_0 - Apparent Area

d - Interference

E – Young's Modulus

E^* - Plane Strain Modulus

F_a - Friction Force

F_n - Normal Force

g - Amplitude of the Sinusoidal Function

H - Height of the Asperity Substrate

Pm - Average Mean Pressure

R - Radius of curvature at the Tip of the Sinusoidal Asperity

R_a - Arithmetic Average Height or Centre Line Average

R_q - Root Mean Square

ε_0, K, n – Constitutive parameters of Swift's hardening law

Y_0, C_y, Y_{sat} – Constitutive parameters of Voce's law

α - Fractional Contact Area

λ - Period of the Surface Waviness

μ - Coefficient of Friction

ν – Poisson's Ratio

ψ - Resistance of the Surface to Plastic Deformation

Acronyms

2D – Two Dimensional

3D – Three Dimensional

CLA – Centre Line Average

DD3IMP – Deep Drawing 3D IMPlicit finite element code

FE – Finite Element

RMS – Root Mean Square

nef – Number of Finite Elements

nnc – Number of Nodes in Contact

1. INTRODUCTION

In the relative motion of solid surfaces we can find a resistance force called friction force (Archard, 1957). The studies about the cause and mitigation of friction go back to Aristotle, 384-322 B. C.. In his book *Physics* is introduced an analogy with the first law of motion: "No one could say why a thing …, in motion should stop anywhere; for why should it stop there rather than here? So that thing will either be at rest or must be moved ad infinitum, unless something more powerful gets in its way". In *On the Heavens*, Aristotle hints at the second and third laws of motion stating "as to the cause of such acceleration… the bodies are endowed with a greater force" and "The agent is itself acted upon by that on which it acts." (Feeny, Guran, Hinrichs, & Popp, 1998). The classic laws of sliding friction were developed by Leonardo da Vinci in 1493, but remained unknown until 1699, when they were published by Guillaume Amontons (Feeny et al., 1998; Hutchings, 2016).

Amontons published the result of his experimental investigation about friction of unlubricated solids. According to his work, the frictional force is directly proportional to the normal load and is independent of the contact area of the surfaces, concluding that the frictional force is always equal to $1/3$ of the normal load. These results are based on the assumption that irregularities on the surfaces of the two bodies interlocked, and the relative motion required lifting the load from one interlocking position to another, which leads to a loss of energy characterized by the arising of a friction force (Bowden & Leben, 1939).

In 1750, Euler adopted the Greek letter μ, for the friction coefficient, which is still used nowadays and define the friction cone, first mentioned by Parent in 1708 (Feeny et al., 1998). Charles-Augustin Coulomb studied the influence of a large number of variables on the friction. He agreed with Amontons on the friction force value being proportional to the load and made a new observation: friction force is independent of the velocity of sliding (Bowden & Leben, 1939). In 1785 Coulomb formulated a law for dry friction, dictating that the magnitude of the kinetic friction is independent of the velocity of sliding. Therefore, the model for kinetic friction was born, based on Coulomb's and Amontons's laws, and is represented by:

$$F_a \leq \mu F_n \tag{1.1}$$

where μ is the coefficient of friction given by the ratio between the friction force (F_a) and the normal force (F_n) (Dupont, 1992).

Coulomb's law is typically used to describe friction between bodies in numerical simulation, which depends only on a single parameter. However, the friction is in fact a very complex phenomenon which also varies with contact pressure, roughness of the surfaces and the velocity of sliding. Thus, it cannot be properly represented by a simple constant value (Feeny et al., 1998).

1.1. Surface Roughness

Most of the surfaces of engineering materials are unavoidably rough. The concept of asperity refers to the set of protrusions that constitutes a roughness surface. Figure 1.1 shows a set of experimentally evaluated asperities on a metallic material, which can be distinguished by their yellow or red colours, depending on their heights. Real surfaces contain geometric irregularities (asperities) with feature sizes ranging over many length scales (Gao, Bower, Kim, Lev, & Cheng, 2006). Surface roughness evaluation is very important for a fundamental problem as frictional contact. It is characterized by protuberances of the surface, i.e. small bumps (peaks) and re-entrances (valleys), which describe the surface: when there are large deviations, it's a rough surface, if the deviations are small, it's a smooth one. The roughness is typically quantified by the parameters R_a and R_q.

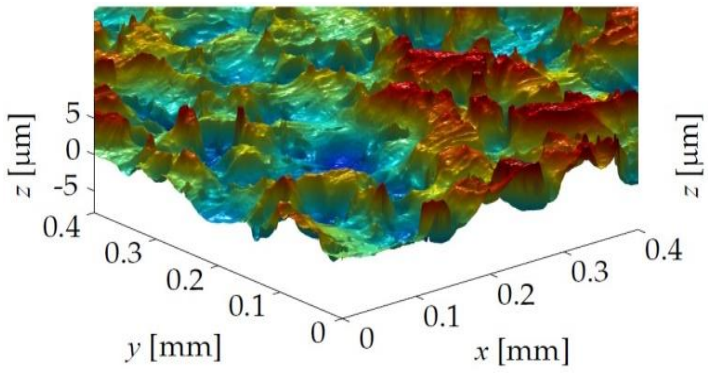

Figure 1.1. Texture of a 3D surface (Hol, Meinders, de Rooij, & van den Boogaard, 2015).

The parameter R_a defines the arithmetic average height, also known as the centre line average (CLA), which is defined by:

$$R_a = \frac{1}{c}\int_0^c \left| z(x) \right| dx, \tag{1.2}$$

where *c* is the sampling length and *z* denotes the function that describes the surface roughness. It defines the average absolute deviation of the roughness irregularities, from the mean line over one sampling length, as represented in Figure 1.2 (Gadelmawla, Koura, Maksoud, Elewa, & Soliman, 2002).

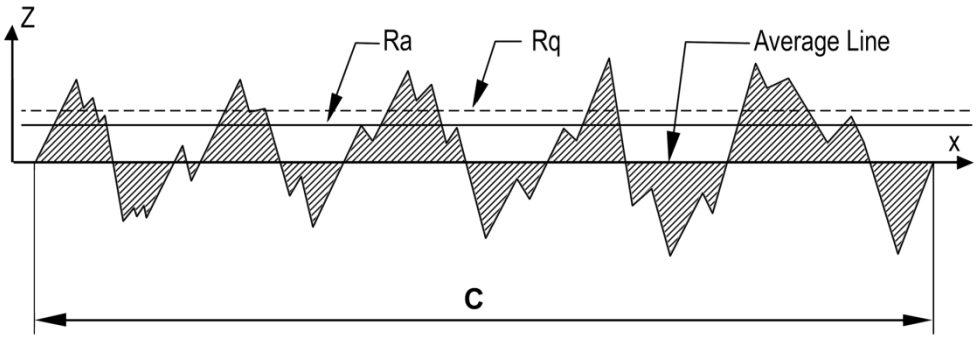

Figure 1.2. Roughness parameters of a surface profile (Silva, Ribeiro, Dias, & Sousa, 2004).

The root mean square roughness (R_q), also known as RMS (equation (1.3)), represents the standard deviation of the distribution of surface heights. It is a more sensitive parameter than the arithmetic average height (R_a) for larger deviations from the mean line (Gadelmawla et al., 2002).

$$R_q = \sqrt{\frac{1}{c}\int_0^c z^2(x) dx} \tag{1.3}$$

Roughness can be quantified by the parameter R_a and qualified into classes, as displayed in Table 1.1.

Table 1.1. Roughness classes (Silva et al., 2004)

Roughness Class	R_a $[\mu m]$
N12	50
N11	25
N10	12.5
N9	6.3
N8	3.2
N7	1.6
N6	0.8
N5	0.4
N4	0.2
N3	0.1
N2	0.05
N1	0.025

1.2. Objectives of the Study and Outline

The main objective of this study is to simulate the contact between rough surfaces, evaluate the elastic and plastic behaviours and explore effects of geometrical and material parameters on critical variables at the yield inception. In order to simplify the analysis, it will only be analysed the case of contact between plane and rough surfaces, whose protuberances are described by sinusoidal functions.

This dissertation is organized into four main chapters. For a better understanding and to improve the readability, this section briefly summarizes the content on each chapter.

Chapter 1 presents the introduction on the subject of study with a brief background on the friction force considerations and their importance on the accurate results in numerical simulation. It proceeds with the clarification on the terms “surface roughness” and “asperity” and how to quantify and qualify it.

Chapter 2 is a brief review on asperities studies carried out since the last century. It is focused focus on the different approaches taken by many authors, their great achievements and difficulties.

Chapter 3 presents the numerical study concerning the surface roughness between an asperity and a flat surface. Two different geometries are considered: the first in two dimensions and a second axisymmetric geometry in three dimensions. This section contains a description of the finite element model developed, comprising the asperity geometry, the finite element mesh and the simulation results. The number of finite elements and boundary conditions required for an accurate simulation are indicated, as well as the material parameters adopted. Each geometrical or material parameter is studied individually to evaluate their influence. The results obtained in this study are analysed and compared with previous studies in literature.

Chapter 4 contains the main conclusions withdrawn from the study presented on previous chapters.

2. REVIEW ON ASPERITIES STUDIES

This section contains a review of the theories and approaches that have been used to understand the surface roughness. In the last century, several researchers have been dedicating their time to comprehend the contact behaviour in both regimes, elastic and plastic (Liu & Proudhon, 2014). It is well known that surfaces are rough on a microscopic scale, which is the base for existence of many problems as sealing, friction, wear, thermal and electrical conductance. This dictates that the effective contact area is extremely small compared to the apparent area (Chang, Etsion, & Bogy, 1987; Ciavarella, Demelio, Barber, & Jang, 2000; Gao et al., 2006; Greenwood & Williamson, 1966).

Hertz (1882) developed an analytical solution for frictionless non-adhesive elastic half-space contact between two bodies. The surface is assumed continuous and non-conforming (Johnson, 1987). In 1966 Greenwood and Williamson cleared the path by introducing the "asperity-based model" which consists in a statistical approach of a rough surface represented by a collection of asperities with spherical tips. In their model, the rough surface is considered isotropic; all the asperities summits have the same radius *R* but their heights vary by a Gaussian distribution; the asperities' peaks do not merge, they are assumed to be widely spaced; only the asperities can be deformed as the bulk suffers no deformation (see Figure 2.1) (Chang et al., 1987; Gao et al., 2006; Greenwood & Williamson, 1966).

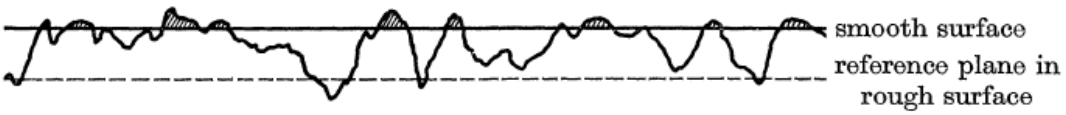

Figure 2.1. Load being supported by the tips of the higher asperities in a contact between a flat and a rough surfaces (Greenwood & Williamson, 1966).

The Greenwood and Williamson model was extended to study curved surfaces (Figure 2.2), using two spheres, considering one of them to be rough (Greenwood & Tripp, 1967). Later, the contact between two flat rough surfaces was analysed, concluding that the

results are equal to the contact between a rough and a flat surface (Greenwood, JA and Tripp, 1970).

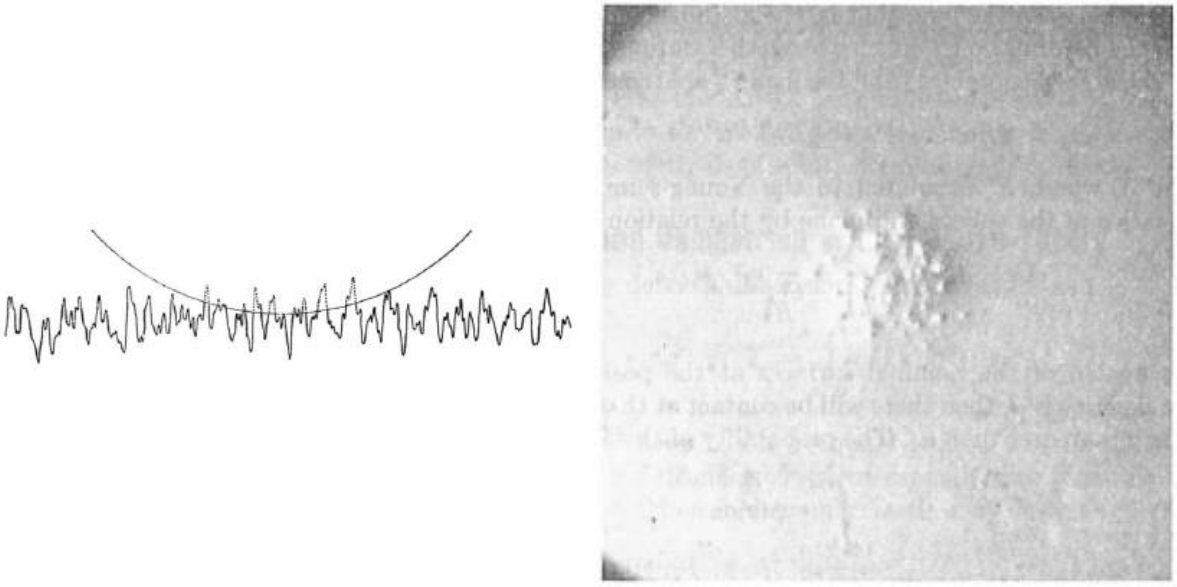

(a) (b)

Figure 2.2. Contact between rough plane and smooth sphere: (a) Surface roughness representation; (b) Contact marks left by a steel ball being pushed against a glass block (Greenwood & Tripp, 1967).

However, it has been difficult to apply the Greenwood-Williamson model to realistic surfaces due to the incapacity to measure accurately the average curvature (distribution of curvature) of asperities, since real surfaces have approximately fractal geometry (Gao et al., 2006). Fractal representation seems to be a perfect fit for describing a real surface topography (Figure 2.3), providing an excellent match to experimentally measured profiles (Gao et al., 2006). The term "fractal" was introduced by Benoit Mandelbrot and is described as a non-Euclidean geometric figure with a never ending pattern displayed at every scale (Mandelbrot & Pignoni, 1983). The first rigorous calculations of elastic contact between surfaces with fractal roughness was performed by Ciavarella et al. (2000). On the other hand, there are some questionable points in their approaches, such as the surface roughness spectrum being perfectly fractal and contacting solids being perfectly plastic (Gao et al., 2006).

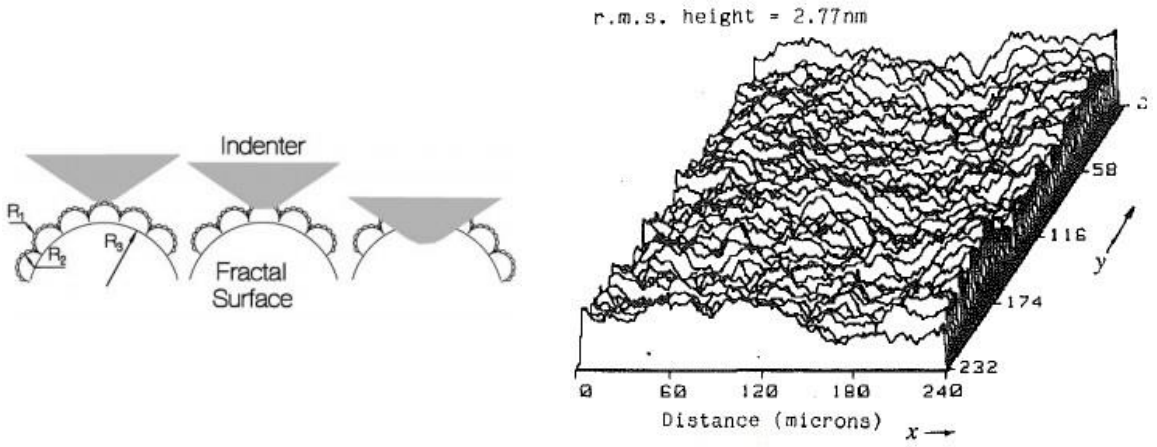

(a) (b)

Figure 2.3. Surfaces with fractal roughness: (a) Schematic of an indenter on a fractal surface (Bobji & Biswas, 1998); (b) Roughness measurements of surface topography (Majumdar & Bhushan, 1990).

Mihailidis, Bakolas, & Drivakos (2001) categorize the models for the determination of real contact area, pressure and surface stress field, in two major categories. The first one has models that treat the real rough surface as a smooth one covered with asperities of known geometry, as in the studies of Greenwood and Ciavarella. This method relies mostly on the Hertzian solution and only the individual asperity deformation is taken into account, neglecting the bulk deformation of the contact bodies. In the second category can be found the models that determine the pressure distribution, the contact area and the subsurface stress field using roughness profiles, which can be obtained by measurements or generated numerically.

Numerical analysis started to be developed in order to model asperities contact for real rough surfaces. Several finite element models were conceived consisting in a large-scale of numerical computations of rough surfaces. The basic principles for digitized measurements from rough surfaces, in numerical elastic contact techniques, were described in detail by Sayles, (1996), for two- and three-dimensional topography data. Polonsky & Keer, (1999) promised a fast numerical method for surface samples with 10^5-10^6 data points (Figure 2.4), that can be solved on a personal computer in a few hours.

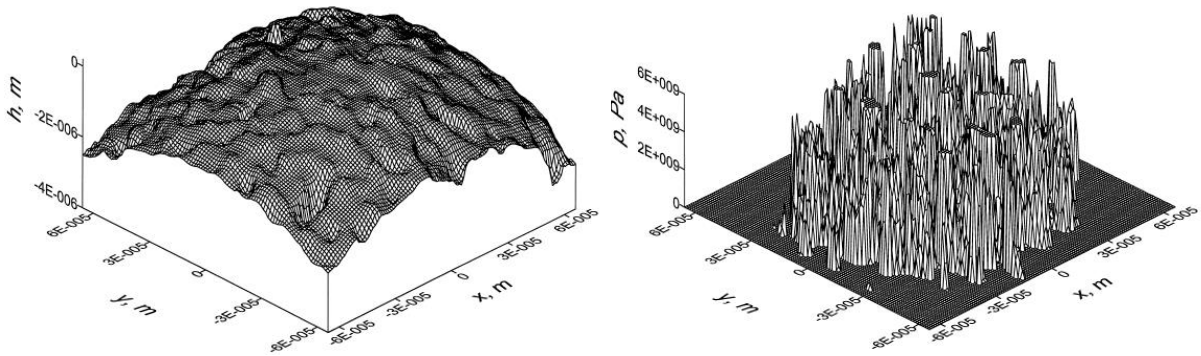

(a) (b)

Figure 2.4. Rough contact problem: (a) Composite shape of the contacting surfaces; (b) Contact pressure distribution (grid dimensions: 121 x 103 nodes) (Polonsky & Keer, 1999).

It is a common approach to model elastic-plastic contact of realistic surfaces recurring to a hybrid scheme, i.e. the bulk and the asperity are modelled separately (Gao et al., 2006). In literature there are models with different shapes of asperities. The typical ones are sinusoidal, paraboloid, ellipsoid and conic, as shown in Figure 2.5. Yastrebov, Durand, Proudhon, & Cailletaud, (2011) compared all the four shapes in matters of contact area and free volume evolutions. As demonstrated in Figure 2.6 (a), the contact area increases linearly with the load rise, presenting identical evolutions for each geometry. In the case of free volume, presented in Figure 2.6 (b), it is clear that, for the largest asperities (with parabolic and elliptical shape), the load required to reach the same free volume is higher than with conic or sinusoidal shapes. It also can be concluded that asperities with a tiny top crush faster than those with a larger summit.

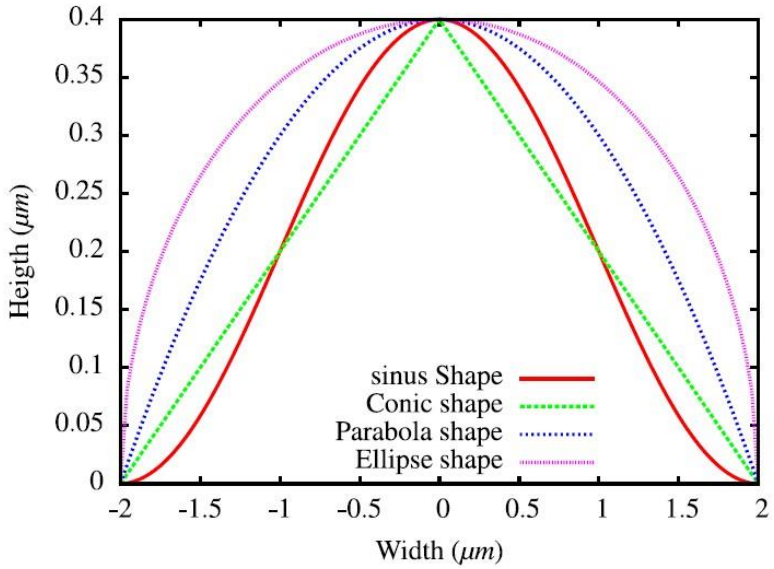

Figure 2.5. Comparative representation of Sinusoidal, Conic, Paraboloid and Ellipsoid shapes (Yastrebov et al., 2011)

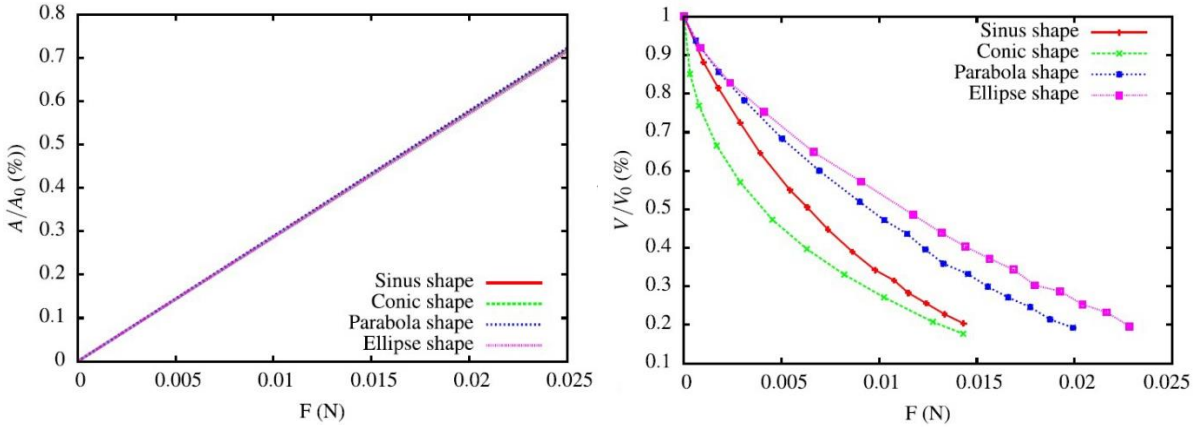

(a) (b)

Figure 2.6. Influence of the shape: (a) Contact area evolution; (b) Free volume evolution (Yastrebov et al., 2011).

Many studies have been showing that the surface roughness can be strongly simplified into a sinusoidal wave function (Bowden & Leben, 1939; Dundurs, Tsai, & Keer, 1973; Gao et al., 2006; Liu & Proudhon, 2014). It is applied to the elastic-plastic contact study between a periodic sinusoidal surface and a rigid flat in two-dimensions (Dundurs et al., 1973; Gao et al., 2006) and an elastic contact in three-dimensions (Liu & Proudhon, 2014).

3. FINITE ELEMENT SIMULATION

The numerical model developed in this study considers a single deformable asperity interacting with a rigid flat surface. Since the contact between two identical rough surfaces is equivalent to the contact between a rigid flat and a rough deformable surface with the combined topography of the two contacting surfaces, its simplification is taken into account (Bucher, Knothe, & Theiler, 2002; Greenwood, JA and Tripp, 1970). The numerical simulations presented in this study were carried out with the in-house finite element code DD3IMP[1] (Menezes & Teodosiu, 2000). An updated Lagrangian scheme is used to describe the evolution of the deformation. In each increment, an explicit approach is used to obtain a trial solution of the nodal displacements and then a Newton-Raphson algorithm is used to correct the first trial solution, which finishes when a satisfactory equilibrium state is achieved. This procedure is repeated until the end of the process. The Newton-Raphson algorithm is used to solve both the non-linearities associated with the friction contact and the elastoplastic behaviour of the deformable body, in a single iterative loop (Oliveira, Alves, Chaparro, & Menezes, 2007).

3.1. Materials

In order to assess the effect of the material behaviour on the asperity deformation, different materials are studied. Therefore, the values assigned to elastic parameters as yield stress σ_y, Young's modulus E and Poisson's ratio υ will vary, taking into account that, for realistic materials, $10 < E^*/\sigma_y < 1000$, where E^* is the plane strain modulus of the substrate, given by (Gao et al., 2006):

$$E^* = \frac{E}{\left(1-\nu^2\right)}. \tag{3.1}$$

[1] DD3IMP- Contraction of "Deep Drawing 3D IMPlicit finite element code" (Menezes & Teodosiu, 2000)

The plastic behaviour of the asperity, namely the hardening law, can be modelled by Voce or Swift hardening laws (see equation (3.2) and (3.3), respectively). In order to simplify the finite element model, the mechanical behaviour of the asperity is assumed linear elastic and perfectly plastic. Thus, it was concluded that both hardening laws can be applied without influence on the results.

$$Y = Y_0 + \left(Y_{sat} - Y_0\right)\left[1 - \exp\left(-C_y \cdot \bar{\varepsilon}^{p}\right)\right] \tag{3.2}$$

$$Y = K\left(\varepsilon_0 - \bar{\varepsilon}^{p}\right)^n \tag{3.3}$$

All the simulations presented in this work considered an elastic (E e υ) and perfectly plastic isotropic material. The hardening law adopted was Voce's (equation (3.2)) and the material parameters are presented in Table 3.1.

Table 3.1. Mechanical properties of the materials used in numerical simulations.

E (GPa)	ν	σ_y (GPa)
600	0.42	5
400	0.4	1
200	0.3	0.6
60	0.2	0.3

3.2. Asperity Geometry

The finite element model is composed of two bodies: a rigid flat surface and a deformable asperity featuring a sinusoidal profile, as shown in Figure 3.1. Only the upper region of the asperity is modelled, since the deformation is limited to the asperity tip and plastic yielding initiating at a very small interference with the rigid body (Liu & Proudhon, 2014). On the other hand, the flat surface is considered perfectly rigid in the numerical model. Thus, only the asperity is described as a deformable body in the numerical model. In this work, the flat surface is discretized with quadrilateral elements and is then smoothed with Nagata patches (D. M. Neto, Oliveira, Menezes, & Alves, 2014). The discretization of the asperity was carried out with isoparametric, 8-node hexahedral finite

elements associated with a selective reduced integration (Hughes, 1980; Menezes & Teodosiu, 2000).

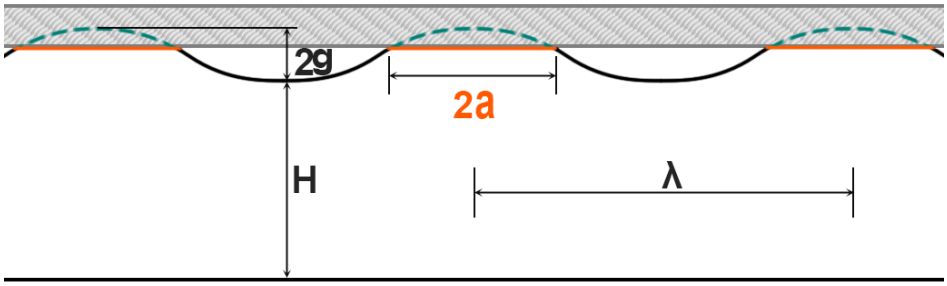

Figure 3.1. Representation of the interaction between the two bodies (Gao et al., 2006).

The rough surface is represented by the sinusoidal periodic function $z(x)$ in equation (3.4). g is the amplitude of the function and, since the referential is fixed at the base of the asperity's tip, the height of the tip is given by $2g$; λ is the period of the surface waviness and H refers to the height of the asperities substrate. To guarantee independence between the tip of the asperities and their substrate, H must be bigger than 3λ (Gao et al., 2006). All the measurement unites are considered in nanometres (10^{-9} m).

$$z(x) = g\cos(2\pi x/\lambda) \quad \text{for} \quad (0 \le x \le \lambda/2) \tag{3.4}$$

According to the definition of surface roughness presented in section 1.1, for a certain sample length, c, its value is given by the arithmetic average height R_a, equation (1.2) and the RMS R_q, in equation (1.3) . Replacing the function $z(x)$ by the expression in equation (3.4), equations (3.5) and (3.6) are obtained.

$$R_a = \frac{2g}{\pi} \tag{3.5}$$

$$R_q = \frac{g\sqrt{2}}{2} \tag{3.6}$$

Based on this information it is concluded that g is the only parameter that influences the surface roughness and the asperity width is not to be taken into account. For realistic materials $0.01 < g/\lambda < 0.1$ (Gao et al., 2006). Asperities may present several shapes, being elongated, flattened or pointed, for example. In sections 3.3 and 3.4, are exhibited the geometries that were adopted, taking into account two different forms of asperities.

3.3. 2D Finite Element Model

The first model analysed considers a two dimensional geometry of an asperity, taken into account plane strain conditions. The asperity model was constructed using the pre-processing software GID® and represents $1/2$ asperity due to symmetry conditions, exercising the principle that all the results are equal for each half, since the asperity has vertical symmetry. With the purpose of studying the influence of the geometry, three different models were constructed with $\lambda = 100\,\text{nm}$ and varying the parameter g (height of the tip), as shown in Figure 3.2. The three values selected in this study are $g = 1$ nm, $g = 5$ nm and $g = 10$ nm. The radius of curvature at the tip of the sinusoidal asperity is obtained by (3.7):

$$R = \frac{\lambda^2}{2\pi^2 g}. \tag{3.7}$$

Considering the three values of the tip height and using equation (3.7), the radius of curvature is exposed in Table 3.2.

Table 3.2. Radius of curvature at the tip for different heights of the asperities.

g [nm]	1	5	10
R [nm]	506.61	101.32	50.66

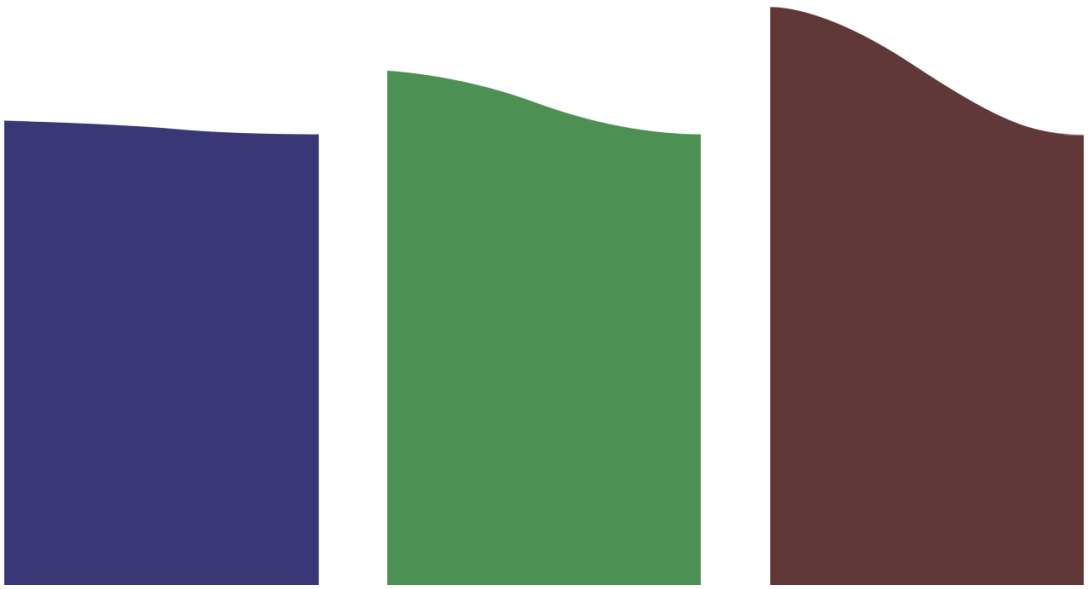

(a) (b) (c)

Figure 3.2. Detail of the asperity's tip's curve, with H=400 nm, varying the parameter g: (a) for g=1 nm; (b) for g=5 nm; (c) for g=10 nm.

The contact surface (sinusoidal) was generated through a parametric surface definition in GID. For the numerical simulation with this geometry, it was used a finite element mesh with approximately 30,000 elements, with a progressive distribution along the vertical direction, refined at the asperity's tip, as shown in Figure 3.3. The computing time ranges between 1.5 to 2.5 hours.

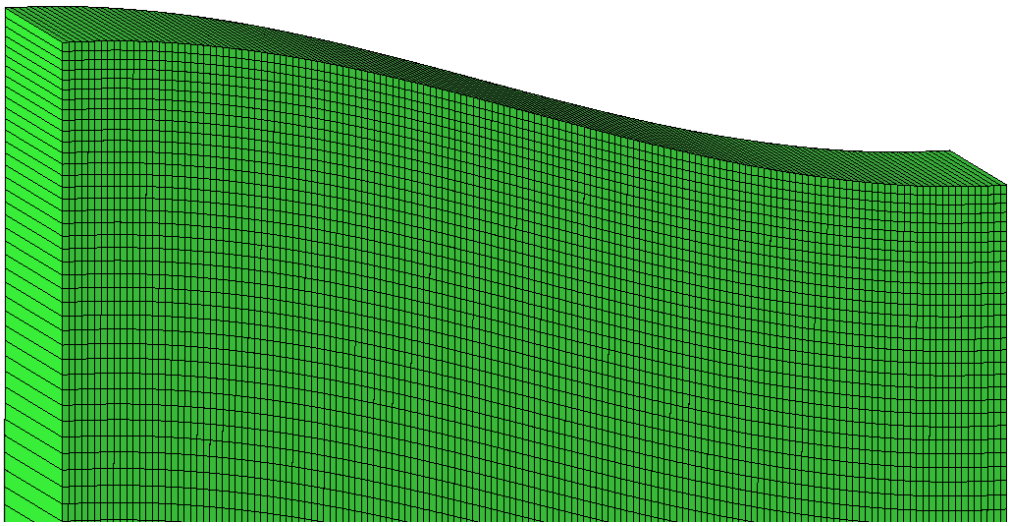

Figure 3.3. Mesh appearance at the upper part of the asperity. Particular attention to the progressive mesh used along the vertical.

3.4. 3D Finite Element Model

The second model, also developed using the pre-processing software GID® considers a three dimensional axisymmetric geometry for the asperity. Due to symmetry conditions, this model illustrates $1/4$ of asperity (Figure 3.4) and allows collecting information on several directions. The contact surface was generated through a parametric line and posteriorly revolved.

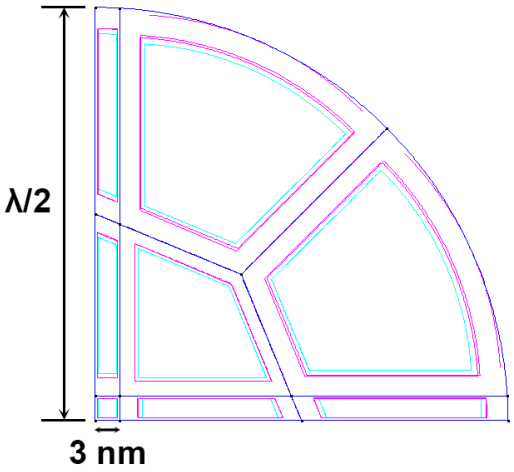

Figure 3.4. Top view of the 3D geometry on GID®.

The plastic yield occurs for a small interference value, thus, for it to be possible to analyse the material behaviour in the elastic regime, a refined finite element mesh at the asperity's tip was necessary (Figure 3.5). Due to the high computational cost associated with a large number of elements, eight volumes were constructed to enable the use of a refined FE mesh just at the tip, about a 3×3 nm square (Figure 3.4), taking into account that all finite elements must be hexahedral. In order to capture detailed information of initial contact, the FE size is about 0.05 nm in the refined square at the asperity's tip. To smooth the transition between FE in different volumes, a progressive mesh was created in order to refine only the tip, for x, y and z directions.

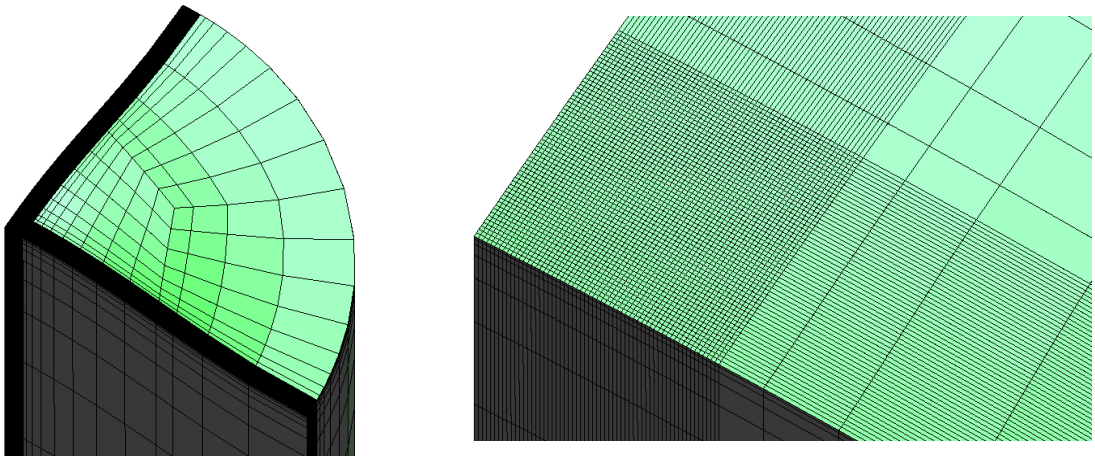

(a) (b)

Figure 3.5. Axisymmetric geometry of the asperity: (a) Concentrated and progressive mesh; (b) Detail of refined zone at the edge of the asperity.

Two models were created, for $g = 5\,\text{nm}$ and $g = 10\,\text{nm}$ (Figure 3.6), with $H = 400$ nm. The radius of curvature R, (see equation (3.7)), are indicated in Table 3.3.

Table 3.3. Radius of curvature at the tip for different heights of the asperities.

g [nm]	5	10
R [nm]	101.32	50.66

Their respective meshes have 62,016 to 87,855 finite elements, for the small value of g, and, for the largest, 144 703 finite elements. This has an adjacent cost of computational time ranging between 3.5 hours to 11.33 hours.

(a) (b)

Figure 3.6. Detail of the asperity's geometry cross-section, varying the parameter g: (a) For g=5 nm; (b) For g=10 nm.

3.5. Boundary Conditions

Considering the 2D[2] model, the contact nodes are contained in the yellow surface of Figure 3.7 (a). The displacement of the nodes is constrained in the x direction, for $x=0$ and $x=\lambda/2$ (green surfaces in Figure 3.7 (a)) and restricted in the y direction for all nodes due to the plane strain deformation mode (burgundy surfaces in Figure 3.7 (b)) . For $z=-H$, at the base of the asperity, the nodes are constrained in z direction (blue surface in Figure 3.7 (a)).

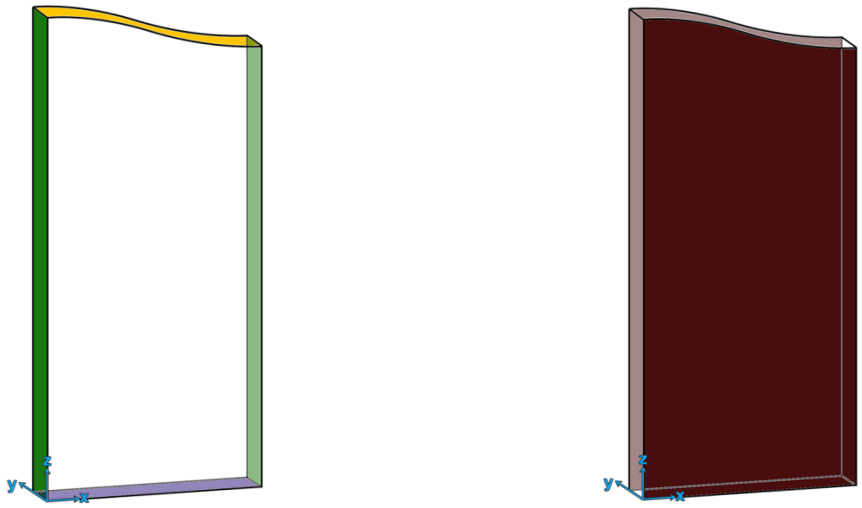

(a) (b)

Figure 3.7. Schemes of the 2D geometry: (a) In yellow is the contact surface and blue the base surface. Green represents the surfaces defined by *x=0* and *x=λ/2*; (b) Surfaces with finite elements constrained in *y* direction.

Considering the 3D[3] model, the nodes located in $x=0$ (green surface in Figure 3.8 (a)) were restricted in the x direction, the nodes located in $y=0$ (blue surface, as shown in Figure 3.8 (a)) were restrained in the y direction, while the cylindrical surface was radially restrained (brown surface in Figure 3.8 (b)). At the base of the asperity, for $z=-H$, the nodes are constrained in z direction (blue surface in Figure 3.8 (c)).

[2] 2D – refers to an entity with two dimensions
[3] 3D – refers to an entity with three dimensions in space

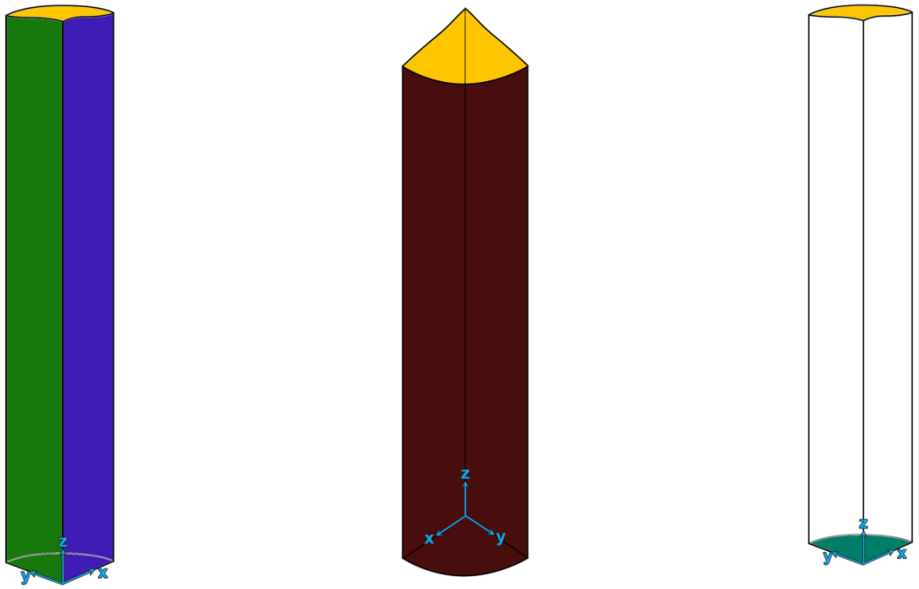

(a) (b) (c)

Figure 3.8. Schemes of the 3D geometry: (a) Blue represents the plane *xz* and green refers to the plane *yz*; (b) Cylindrical surface marked with brown; (c) The top surface is yellow and the base is blue.

In both cases (2D and 3D models), the flat surface is initially fixed at $z = 2g$ and then is pressed downwardly against the asperity's tip, as represented in Figure 3.9. There is no friction between the rigid plane and the sinusoidal asperity.

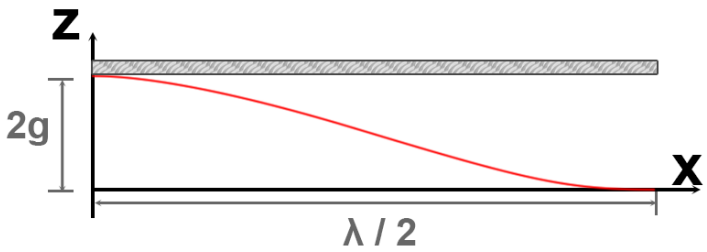

Figure 3.9. Scheme of the two parts model and positions.

After the parametric models are constructed, the parametric FE meshes created and the boundary conditions defined, simulations are ready to proceed. The computer used had the following characteristics:

Processor:	Intel®Core™ i7-5930K CPU @ 3.50GHz
Installed memory (RAM):	64.0 GB
System type:	64-bit Operating System

3.6. 2D Simulation

The contact between the asperity and the flat surface leads to an increasing affective contact area, A_r, which is represented by the red zone in Figure 3.10 (a). In the same figure it is possible to define the parameter a, the half-width of the contact area, which is a distance measured in the x direction and can be obtained by:

$$a = \left(\frac{\lambda / 2}{nef} \right) \cdot \left(\frac{nnc}{2} - 1 \right) \tag{3.8}$$

where *nef* is the number of finite element in *x* direction and *nnc* denotes the number of finite element nodes in contact with the rigid surface. Figure 3.10 (b) presents the vertical displacement of the edge of the asperity's tip, called interference, d. The value of the interference is directly linked with the vertical displacement of the flat rigid surface. All the numerical simulations presented in this section were conducted until the sinusoidal surface reached full contact with the rigid surface.

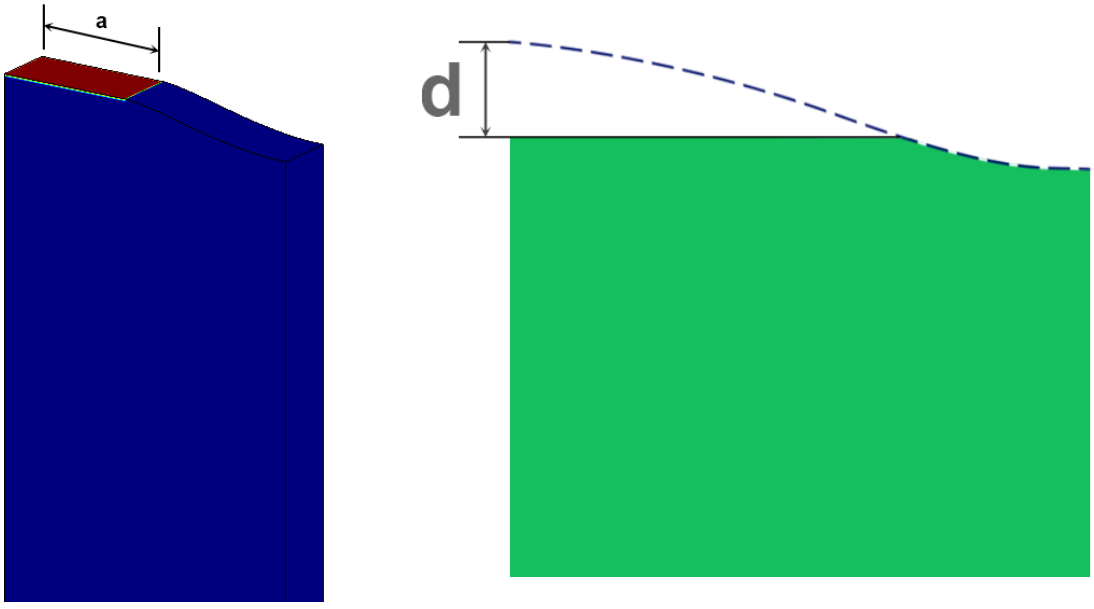

(a) (b)

Figure 3.10. Criteria to study the contact between surfaces: (a) Contact area and contact length; (b) Interference.

3.6.1. Influence of the Geometry

Just as it was discussed in section 3.2, g (height of the tip) seems to be the only geometrical parameter with influence on the surface roughness. Consequently, three different values were attributed to g (Figure 3.11).

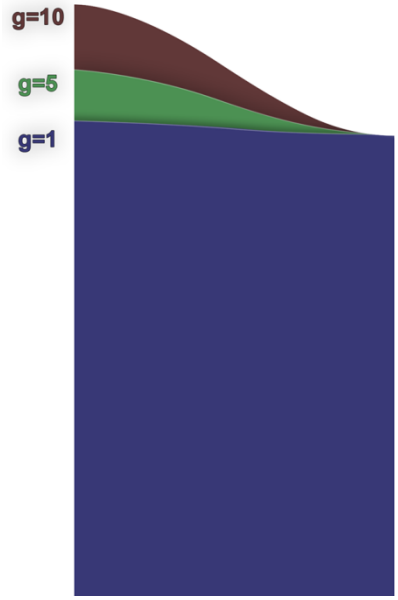

Figure 3.11. Overlap of the three different asperities in this study.

Table 3.4. Mechanical properties of the materials used to study the role of geometry in surface roughness.

E (GPa)	ν	σ_y (GPa)
60	0.3	3 0.6 0.3

The mechanical properties of the materials used to study the asperity deformation are presented in Table 3.4. The influence of the parameter g on the average mean pressure, *Pm*, predicted by finite element simulations is presented in Figure 3.12. *Pm* is obtained by the ratio between the force applied by the rigid plane on the asperity's tip and the real contact area, A_r. Comparing the blue curve, for $g = 5\,\text{nm}$, and the red curve, with $g = 1\,\text{nm}$, it is verified that, for the same value of σ_y, the average mean pressure is always higher for the highest value of g (blue line). For the largest σ_y (Figure 3.12 (a))

it's observed the higher mean pressure as for the small σ_y the pressure value registered is the smallest (Figure 3.12 (c)).

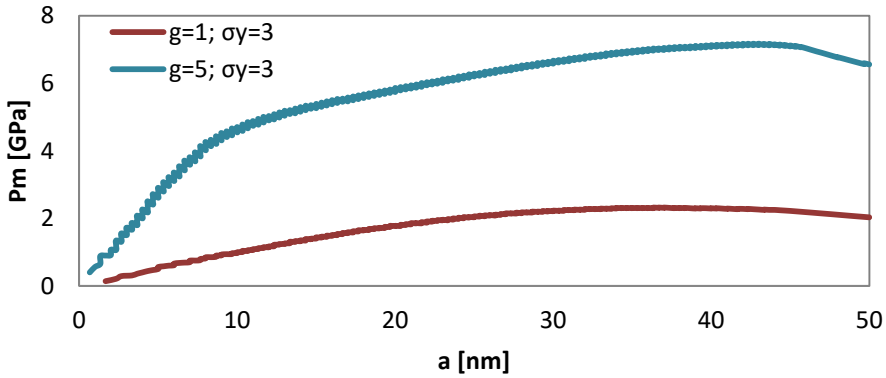

(a)

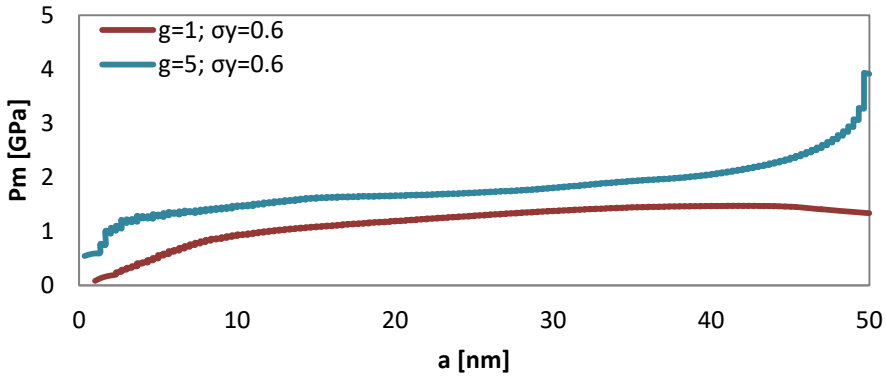

(b)

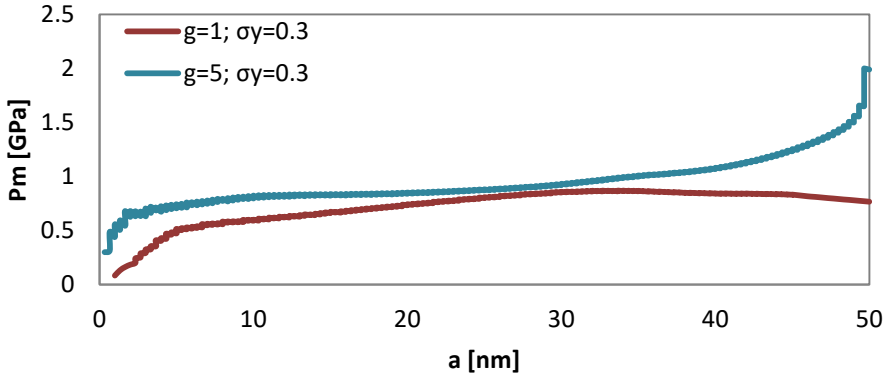

(c)

Figure 3.12. Influence of the asperity's geometry on the mean pressure as a function of the contact radius: (a) with σ_y=3 GPa; (b) for σ_y=0.6 GPa; (c) Considering σ_y=0.3 GPa.

3.6.2. Influence of the Material

This section intends to display effects of material parameters on the variation of the average mean contact pressure, during elastic and initial plastic deformations. Table 3.4 shows the material parameters considered to find out the role of σ_y in elastic and initial plastic deformations and its effect on the applied load.

The relationship between the average asperity contact pressure and the half-width of the contact (a) can be analiticaly defined assuming elastic behaviour of the material (Gao et al., 2006):

$$Pm = \frac{\pi \sin^2(\pi\alpha)}{2\alpha} \cdot \frac{gE^*}{\lambda} \tag{3.9}$$

where g, λ and E^* are well known constant values and α, the fractional contact, is obtained by:

$$\alpha = \frac{a}{\lambda}. \tag{3.10}$$

This relationship is represented by the black curve in Figure 3.13, which is almost coincident with the numerical result for g=1 nm and $\sigma_y = 3$ GPa. This asperity's geometry and material allows the entire deformation of the asperity in the elastic regime. On the other hand, for g=5 nm and $\sigma_y = 0.3$ GPa, the numerical curve diverges quickly from the analytical tendency, as shown in Figure 3.13 (b). This occurs because the plastic strain arises early, leading to an almost constant average asperity contact pressure. The numerical simulation curves are coincident with the analytical solutions curves at an early stage, while there is elastic deformation. When the material starts to shows plastic behaviour, the curve obtained by simulation deviates from the analytical solutions. For the same values of yield stress it is concluded that, for a higher asperity, the plastic behaviour initiates at a smaller contact than smaller asperities.

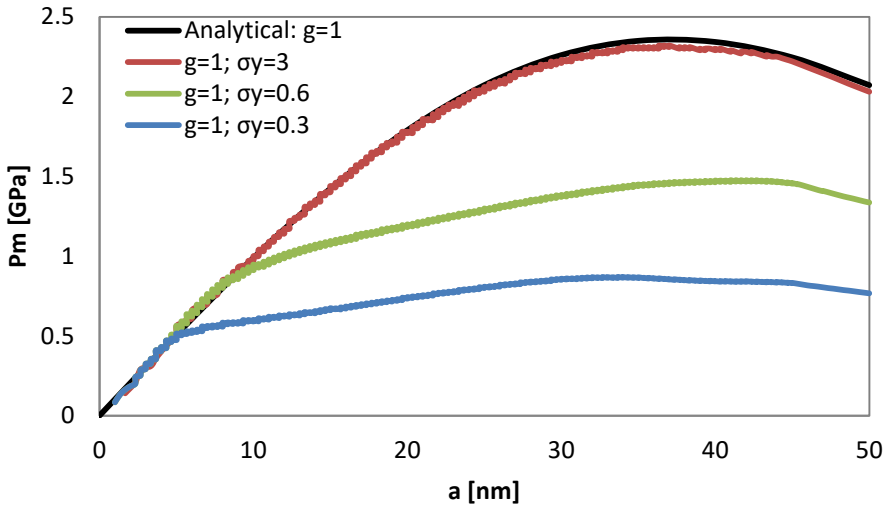

(a)

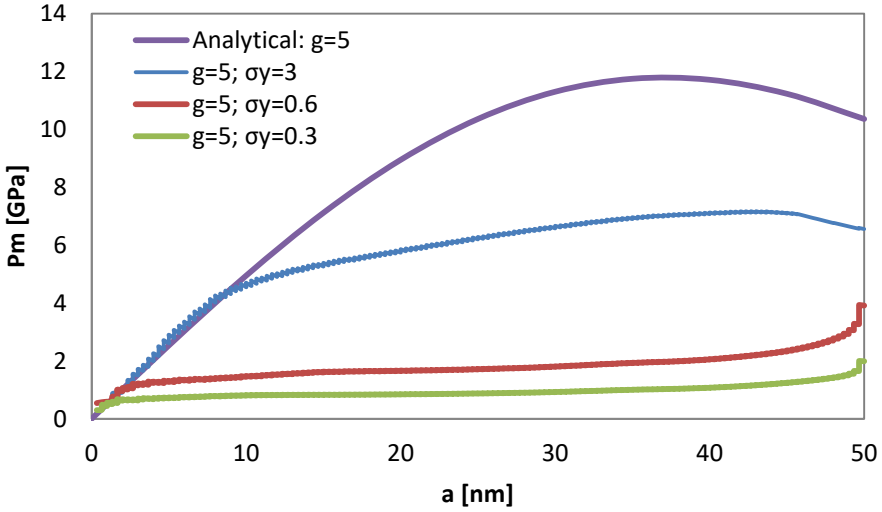

(b)

Figure 3.13. Influence of the height of the tip on the mean asperity contact pressure as a function of the half-width of the contact: (a) Geometry with g=1 nm; (b) Geometry with g=5 nm.

The mean contact pressure evolution is shown in Figure 3.13 (a), for the small value of the height of the tip (g=1 nm), and Figure 3.13 (b) for the largest one (g=5 nm). A tendency it's observed for the mean pressure to be higher when the geometry's tip is larger for the same value of yield stress. When the material transitions from the elastic to the elastic-plastic behaviour it is noticed that the mean pressure tends to stabilize until $a \approx 45$ nm, when the neighbouring material starts to interfere.

Table 3.5 indicates the values attributed to every material in four different simulations, namely the change of the Young's modulus, *E*.

Table 3.5. Mechanical properties of the materials considered to study the influence of Young's Modulus.

E (GPa)	ν	σ_y (GPa)
600 400 200 60	0.3	3

The mean pressure tends to have a similar behaviour for materials with higher Young modulus, considering that all *Pm* values stabilize for $10 < a < 18$ nm. However, the lower value of *E* leads to a *Pm* evolution that reaches the plateau later, as shown in Figure 3.14. When the Young's Modulus presents a small value (*E*=60 GPa), the mean contact pressure never reaches the same *Pm* values as those obtained with higher values of *E*, because the elastic regime of deformation is more significant. Moreover, *E* has impact in the transition between elastic and plastic behaviour: the bigger is the Young's Modulus, the lower is the contact (*a*) for which the transition occurs.

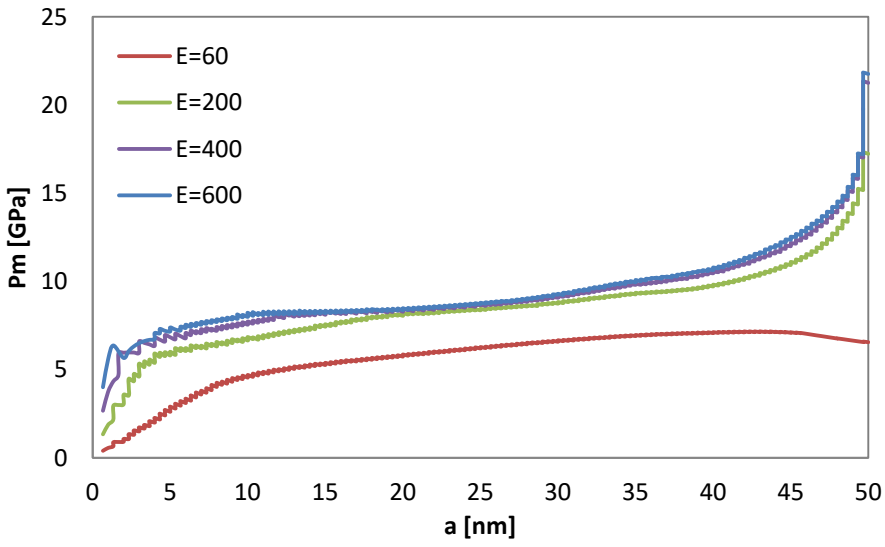

Figure 3.14. Mean pressure evolution as a function of the half-width of the contact, for different values of Young's Modulus, with g=5 nm and σ_y=3 GPa. Plastic behaviour occurs: for E=60 GPa at a≈8 nm; for E=200 GPa at a≈3 nm; for E=400 GPa at a≈2 nm; for E=600 GPa, at a≈1 nm.

Poisson's ratio (i.e. the ratio between transverse strain and axial strain is known to represent elastic compressibility (Liu & Proudhon, 2014). In order to assess the effect of the Poisson's ratio on the numerical solution, the values considered for the materials used in these simulations are listed in Table 3.6. The mean pressure evolution as a function of the half-width of the contact is shwon in Figure 3.15 for different values of Poisson's ratio. This parameter has a small influence on the contact radius (a) at the transition between elastic to plastic regimes (7<a<9 nm). On the contrary, mean pressure increases as bigger is υ at yielding and at the maximum value obtained.

Table 3.6. Mechanical properties of the materials used to study the importance of Poisson's ratio, υ, in the material response.

E (GPa)	ν	σ_y (GPa)
60	0.4 0.3 0.2	3

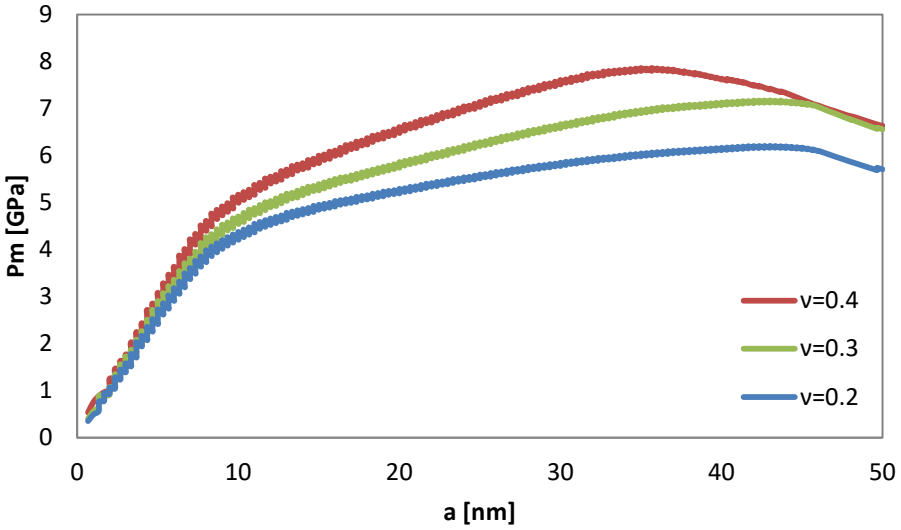

Figure 3.15. Mean pressure evolution as a function of the half-width of the contact, for different values of Poisson's ratio, with g=5 nm and σ_y=3 GPa. Plastic behaviour occurs when the gradient changes, between 7<a<9 nm.

3.6.1. Results and Discussion

Gao et al., (2006) shows that, in general, characteristics of deformation can be made explicit primarily by two dimensionless parameters: α, the fractional contact, which characterizes the extent of contact, and ψ, which characterizes the resistance of the surface to plastic deformation (equations (3.10) and (3.11), respectively):

$$\psi = \frac{E^* g}{\sigma_y \lambda} \tag{3.11}$$

To fully characterize the behaviour it is important to take into account ν and a fourth variable, which could be either E/σ_y or g/λ (Gao et al., 2006).

Figure 3.16 plots the results of the simulations, represented by the points, which shows the critical value of α required to initiate plastic yield, as a function of the dimensionless parameter ψ. These results are valid only for $0 < \alpha < 0.5$. A tendency can be observed by the asymptotic limits $\alpha \to 0$ and $\psi \to 0.265$, as documented by Gao et al. (2006), which gives an approximate estimate of the elastic limit by the condition $\psi\alpha = 0.1$ (yellow line in Figure 3.16), for practical purposes. These results corroborate his theory that the transition from elastic to elastic-plastic behaviour ($\psi < 2$) can be determined only by the values of α and ψ.

Gao et al., (2006) reported two distinct types of behaviour, depending on the value of material parameter ψ:

- for $\psi < 2$ the contact transition from elastic to elastic-plastic behaviour, as α increases, never reaching full plasticity (Figure 3.17 (a)).
- for $\psi > 2$ (Figure 3.17) where there are four different regimes of behaviour: for a small α it is observed an elastic response, then a transition to elastic-plastic behaviour occurs (Pm increases monotony), followed by a constant plateau (the material hardness), and lastly, the contact pressure begins to rise sharply, consequence of the restrictions provided by the neighbouring.

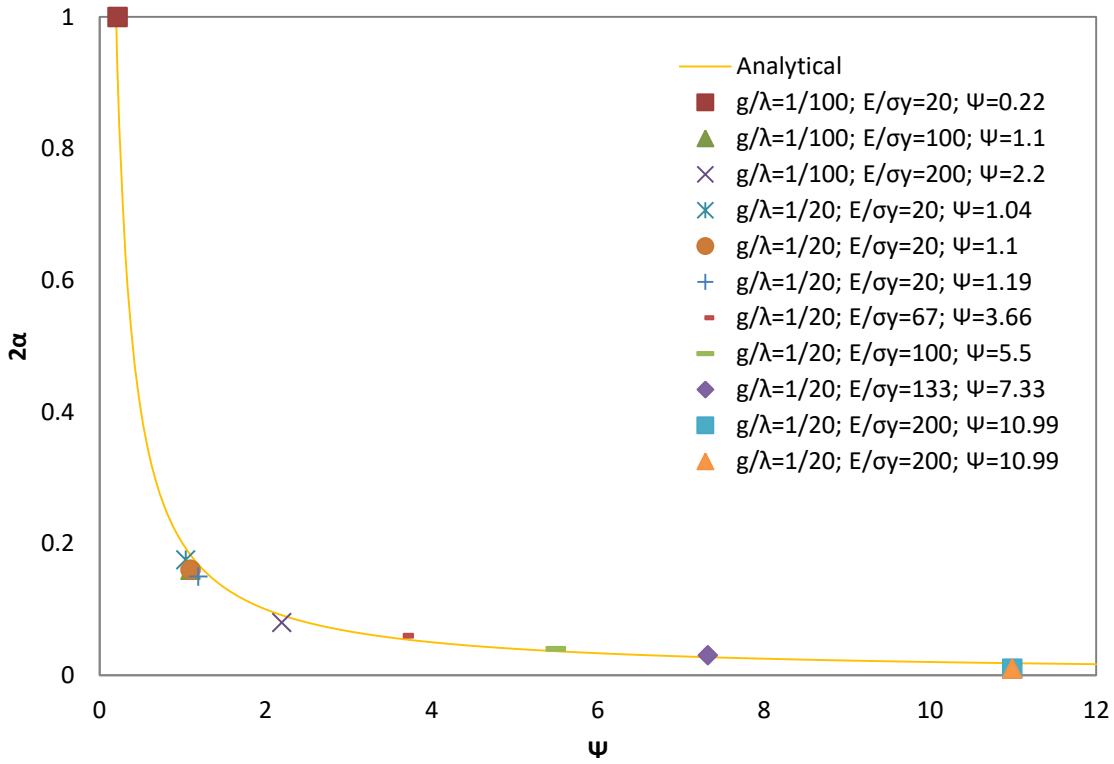

Figure 3.16. Critical value of α required to initiate yield as a function of the dimensionless parameter ψ. The points show the results of finite element simulations and the line demonstrate an asymptotic solution to approximate an estimate of the elastic limit.

Figure 3.17 (a) shows the average asperity contact pressure as a function of contact fraction α for $\psi < 2$. Although ψ determines the general behaviour of the contact, it is noticed that the detailed response of the asperities depends on both E/σ_y and g/λ. For a small α, the asperities begin to interact elastically, then a transition to a regime of elastic-plastic behaviour occurs, with the mean pressure increasing slowly until it reaches its maximum, when the zone of neighbouring asperities begins to interact, ($2\alpha \approx 0.7$) (Gao et al., 2006).

For the second case, in Figure 3.17 (b), it's exposed the mean asperity contact pressure as a function of the contact fraction for $\psi > 2$, with material properties and loading conditions up to full plasticity. In this case, it is noticed no influence of the parameter E^*/σ_y for $2\alpha = 0.5$ and a weak influence for the behaviour transitions. The transitions to the "interacting asperities regime" begins at $2\alpha \approx 0.75$. In a careful observation of Figure 3.17 (a), it is possible to notice that some of the numerical simulation curves deviate slightly from the theoretical curve. This fact is attributed to the method used

to obtain the value a, from an approximate calculations considering the number of contact nodes at every moment based on the formula (3.8).

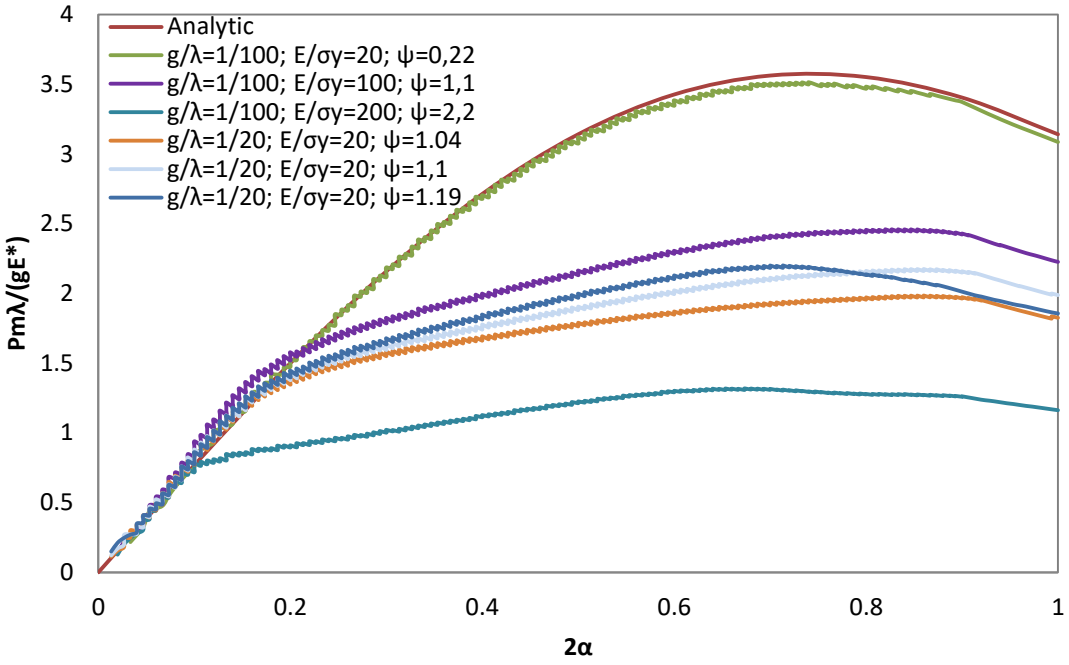

(a)

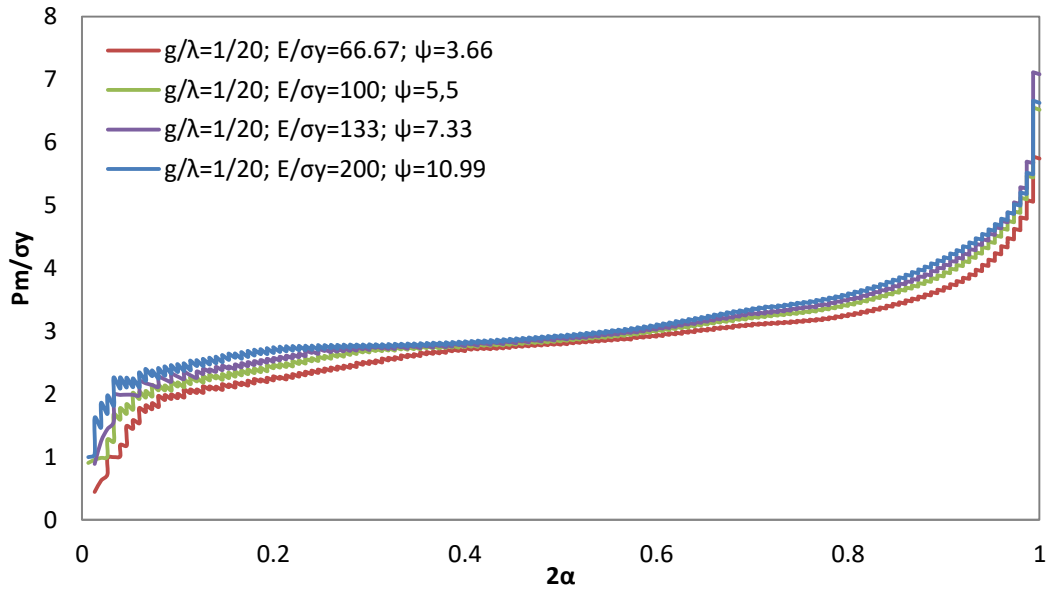

(b)

Figure 3.17. Importance of α and Ψ in controlling the behaviour of a solid (a) Mean asperity contact pressure (normalized by E^*g/λ) as a function of contact fraction for $\Psi < 2$; (b) Mean asperity contact pressure (normalized by σ_y) as a function of contact fraction for $\Psi > 2$.

The contact pressure distribution is presented in Figure 3.18 for the same geometry and varying the yield stress. On the other hand, contact pressure distribution is

presented in Figure 3.19 for the same σ_y and for a different geometry. The maximum value of the contact pressure occurs always in the middle of the asperity, which increases as the interference increases. For low values of interference and consequently elastic deformation regime, the contact pressure distribution presents an elliptic shape, such as in Hertz theory. The contact pressure, progressively, approaches a uniform distribution as ψ increases since the elastic regime is reserved for small values of α and as soon as the neighbouring interactions begin, the contact pressure approaches a constant distribution, as it happens in Figure 3.19 (b). Just as it was expected, comparing Figure 3.18 (a), $\sigma_y = 3$ GPa, (b), $\sigma_y = 0.6\,\text{GPa}$, and (c), $\sigma_y = 0.3$ GPa, the value of the contact pressure distribution decreases with the decreasing of σ_y. The simulations in Figure 3.19 exhibit the contact pressure distribution to reach the total contact between the flat and the sinusoidal surfaces, for g=1 nm, Figure 3.19 (a) and *g*=5 nm Figure 3.19 (b). As well as a greater interference is needed for the highest asperity, it also requires a larger contact pressure.

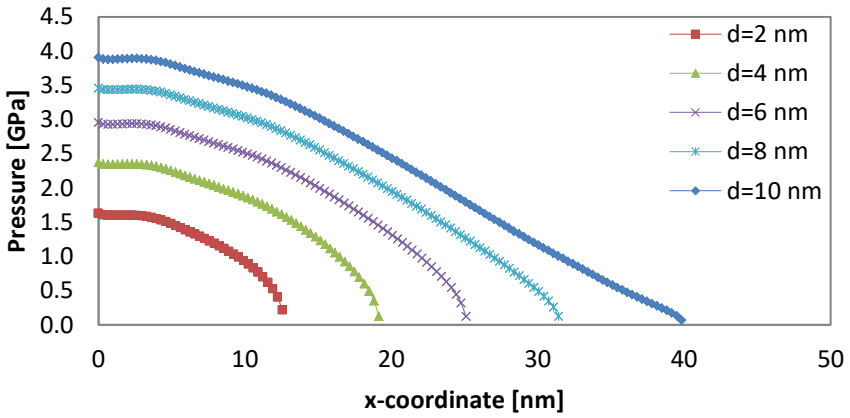

(a)

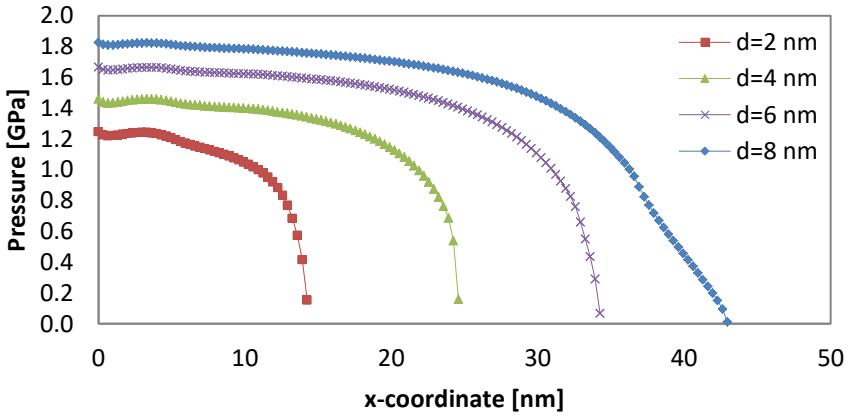

(b)

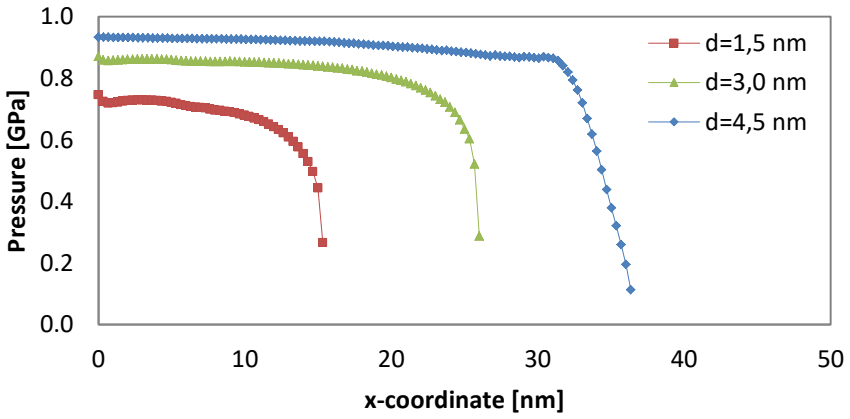

(c)

Figure 3.18. Asperity contact pressure distribution for g/λ=1/100: (a) E/σ_y=20, ψ=0.22; (b)E/σ_y=100,ψ=1.1; (c)E/σ_y=200, ψ=2.2.

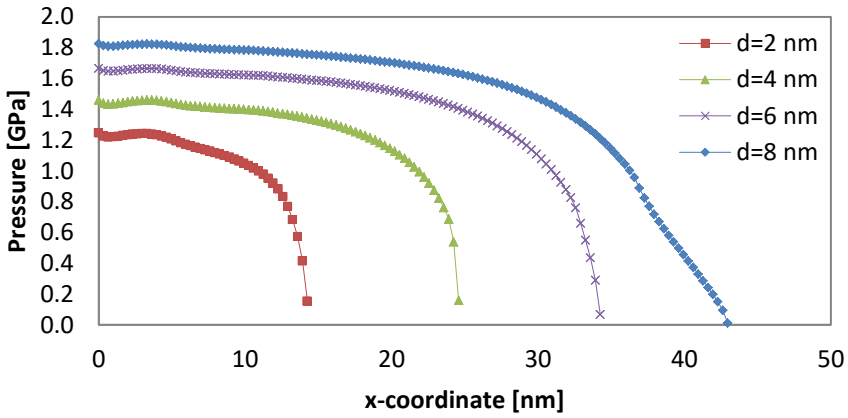

(a)

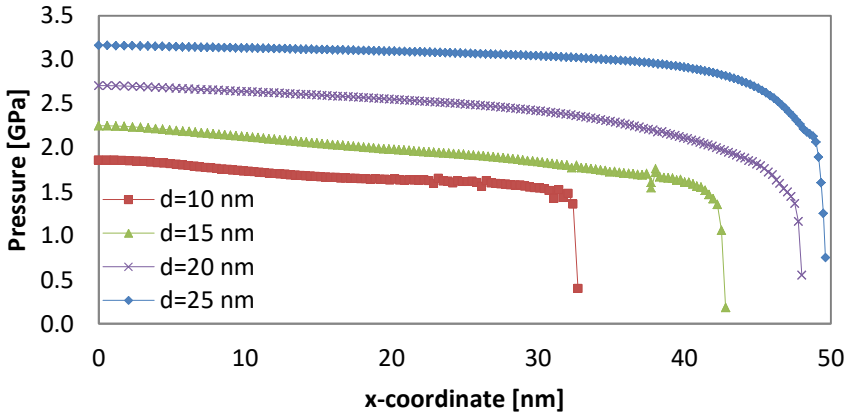

(b)

Figure 3.19. Asperity contact pressure distribution for E/σ_y=100: (a) g/λ=1/100, ψ=1.1; (b) g/λ=1/20, ψ=5.5.

From the contact between the flat surface and the sinusoidal surface of the 2D geometry results a rectangular contact area, A_r. Hertz proposed a theory involving two cylinders with parallel axes that allows describing the elastic contact between both solids. Since the contact area is equivalent, an attempt was made to describe the elastic-plastic behavior, in this case, studied by the Hertz theory. Since small plastic deformations do not alter contact responses, Hertz theory can be applied to deformation with a strain as large as 10% and *a* must be small compared with the radius of curvature (Liu & Proudhon, 2014). The analytical contact pressure distribution is given by (D. M. S. Neto, 2014):

$$p_n(x) = \frac{2f}{\pi b^2}\sqrt{\left(b^2 - x^2\right)} \quad \text{for } x < b \tag{3.12}$$

where f is the force applied, r the radius of curvature and b is the half-width of the rectangular contact surface, obtained by:

$$b = 2\sqrt{\frac{fr\left(1-\upsilon^2\right)}{\pi E}}\,. \tag{3.13}$$

The contact pressure predicted by numerical simulation is presented in Figure 3.20 (a), while the solution given by the Hertz theory is presented in Figure 3.20 (b). The comparison between them show that the elastic-plastic response cannot be predicted by the Hertz theory. Also Liu & Proudhon (2014) suggest that the difference between sinusoidal contact and Hertz solution is due to the non-uniform curvature of the contacting profile.

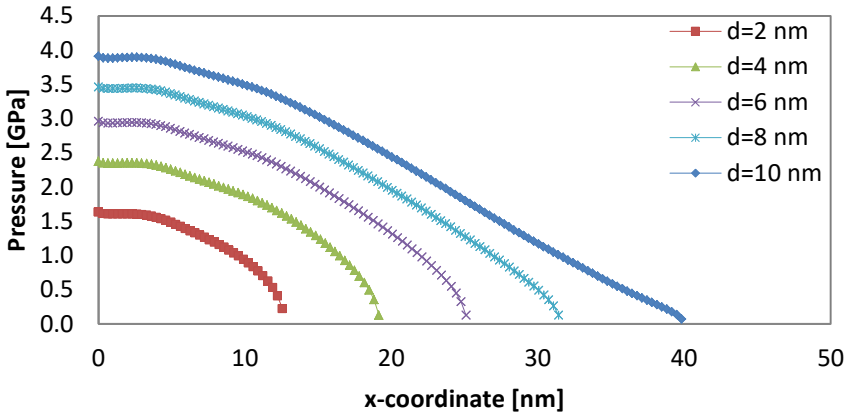

(a)

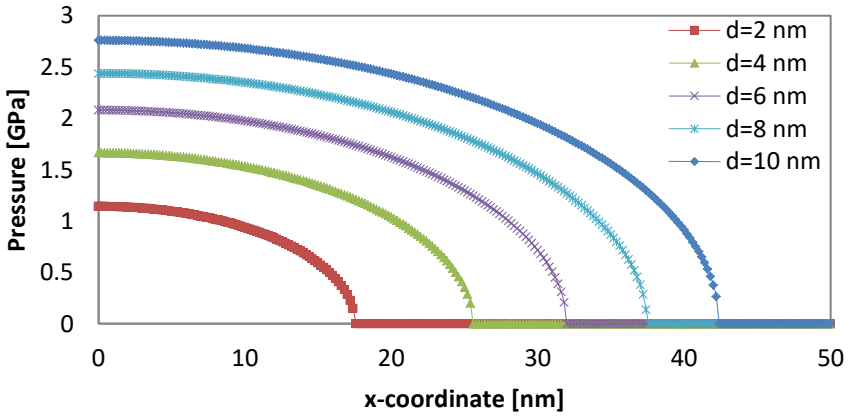

(b)

Figure 3.20. Asperity contact pressure distribution for g/λ=1/100; E/σy=100; ψ=1.1: (a) Values obtained by numerical simulation; (b) Theoretical values given by Hertz theory.

Table 3.7. Mechanical properties of the materials used in simulations for g=10 nm.

E (GPa)	ν	σ_y (GPa)
60	0.3	3
		0.6
		0.3

Although the geometry with $g = 10\,\text{nm}$ was also been built with the material parameters in Table 3.7, the obtained results were the ones considered in the analysis. Increasing the interference due to the flat plane compression, an amount of material was forced to drain to the empty space on the right side. Thus, the developed model of the asperity with the largest tip presents a great amount of material to be displaced. When this material reached the vertical surface, the nodes on the contact surface weren't constrained to the horizontal displacement for $x = \lambda/2$ so they kept moving with the continuous vertical displacement of the flat surface (see Figure 3.21). Therefore, the results obtained weren't comparable with the others due to a limitation in finite elements simulation.

(a)

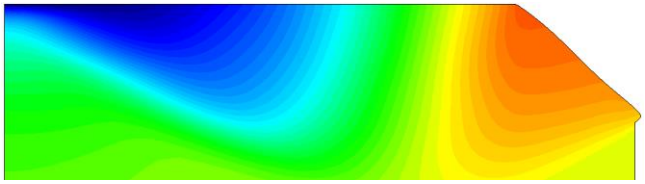

(b)

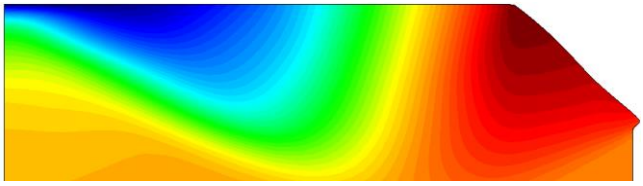

(c)

Figure 3.21. Vertical displacement for g=10 nm: (a) σ_y=3 GPa; (b) σ_y =0.6 GPa; (c) σ_y =0.3 GPa.

3.7. 3D Simulation

From the contact between the asperity and the flat surface results a real contact area - A_r - (represented by red in Figure 3.22 (a)). In the same figure it is possible to define the parameter a , called contact radius, which is a distance measured in x direction, given by the intersection of the plane xy and the plane defined by the contact area. In Figure 3.22 (b) it is observed the interference, represented by d . In order to define the transition between elastic and elastic-plastic regimes, it's considered yield inception whenever a nonzero equivalent plastic strain appears (about 10^{-6}).

(a) (b)

Figure 3.22. Criterions to study the contact between surfaces: (a) Contact area and contact radius; (b) Interference.

3.7.1. Influence of the Geometry

In section 3.4 were introduced two different geometries (see Figure 3.23) to evaluate the elastic and plastic behaviours when subjected to a contact loading. Since g seems to be the only geometrical parameter with influence on the value of surface roughness, as observed in section 3.2, two different values were attributed to it, as shown in Figure 3.23.

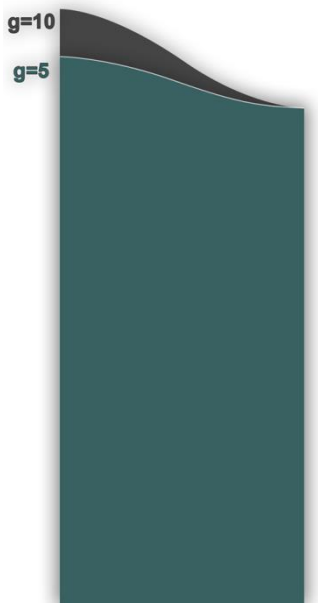

Figure 3.23. Overlap of the two different asperities in study.

Table 3.8. Mechanical properties of the materials used to study the role of geometry in surface roughness.

E (GPa)	ν	σ_y (GPa)
60	0.42	1
		0.6
		0.3

Table 3.8 indicates the characteristics of materials used in these simulations. Figure 3.24 presents the influence of the tip's height on the mean contact pressure in three different cases: (a) for σ_y =1 GPa; (b) for $\sigma_y = 0.6$ GPa; (c) for $\sigma_y = 0.3$ GPa. The blue line corresponds to $g = 5$ nm and the red line refers to $g = 10$ nm. In these three cases it is possible to conclude that the mean pressure, at the yield inception, is similar for different values of g, since σ_y is kept constant. The mean pressure is higher for larger values of σ_y. For the same geometry it is verified that yield inception occurs for smaller values of *a* as the σ_y decreases. The contact radius values presented in this figure are obtained measuring the distance between nodes in contact. Due to the coarse mesh the values aren't always as precise as it should be, creating an uneven evolution. The dashed line indicates when the material behaviour alters from elastic to plastic and how it prograde in plastic regime.

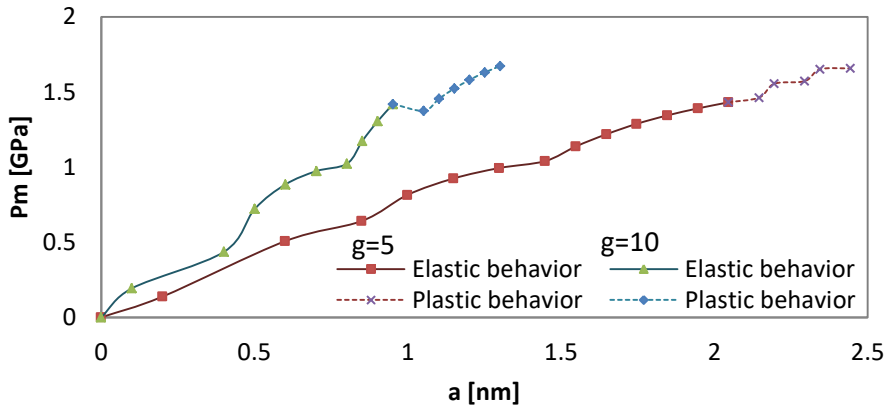

(a)

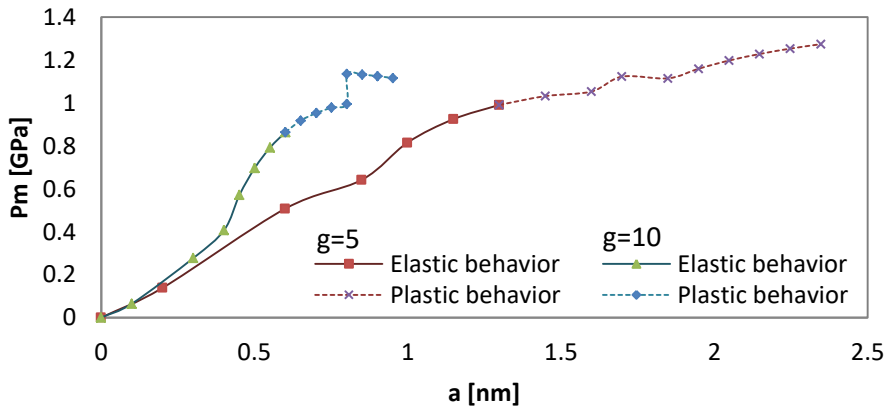

b)

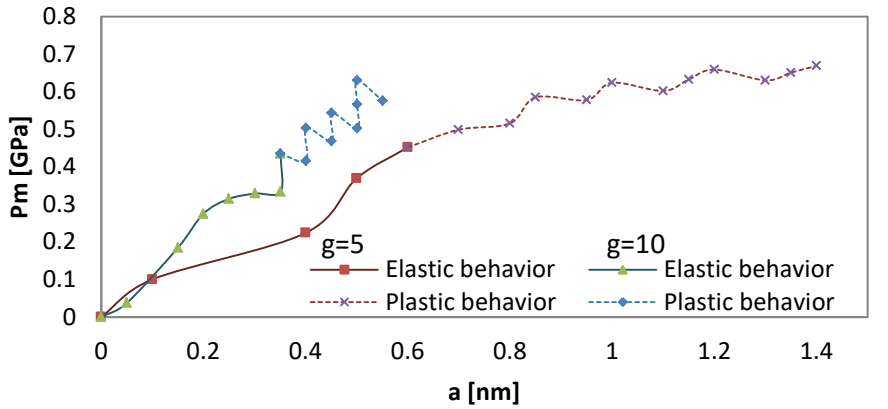

(c)

Figure 3.24. Influence of the asperity's geometry on the mean pressure as a function on the contact radius: (a) with σ_y=1 GPa; (b) for σ_y=0.6 GPa; (c) Considering σ_y=0.3 GPa.

3.7.2. Influence of the Material

This section intends to display effects of material parameters on the variation of the mean contact pressure, during elastic and initial plastic deformations. In order to observe the influence of the yield stress in the material behavior, this parameter was selected ranging between the values indicated in Table 3.8.

The contact radius values presented in this section figures are obtained measuring the distance between nodes in contact. Due to the coarse mesh the values aren't always as precise as it should be, creating an uneven evolution. The dashed line indicates when the material behaviour alters from elastic to plastic and how it evolves in plastic regime.

The evolution of the mean contact pressure is given in Figure 3.25 (a) for $g = 5\,\text{nm}$ and in Figure 3.25 (b) for $g = 10\,\text{nm}$. For the same height of the asperity's tip it is clear that yield stress has a large influence since the transition between regimes occurs for distinct values of *a*. At yield inception, the contact radius seems to be higher for larger values of g and increases with the increasing of σ_y.

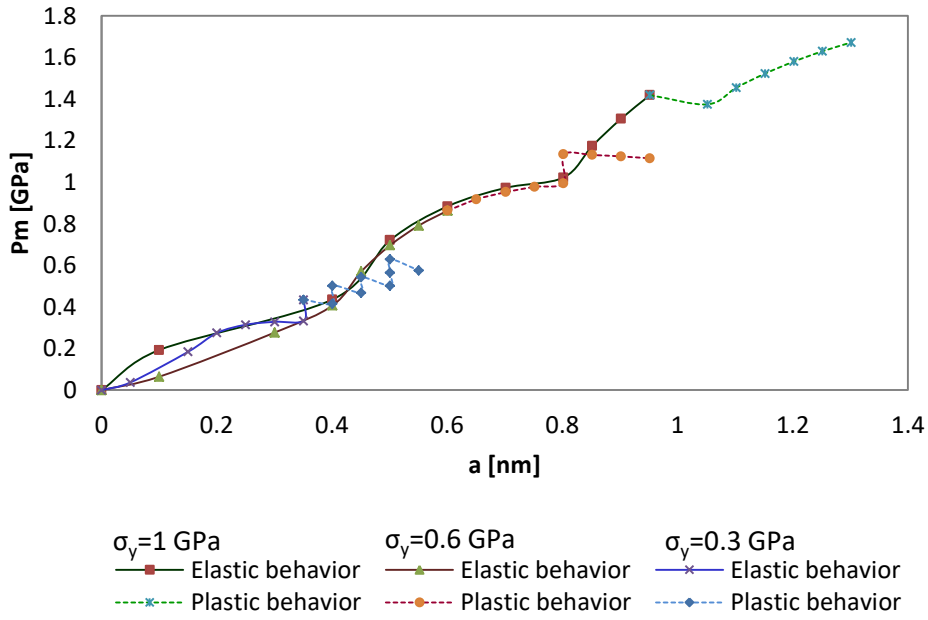

(a)

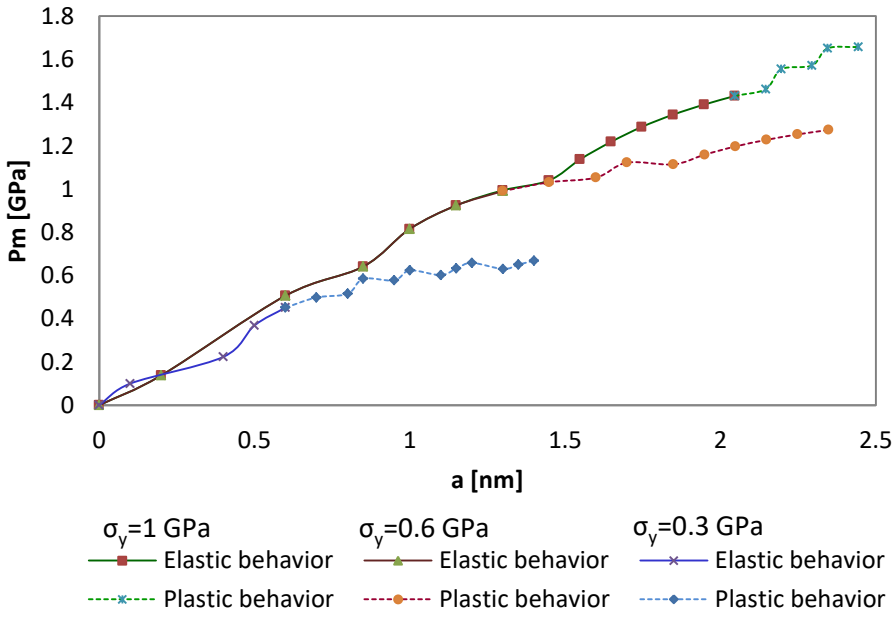

(b)

Figure 3.25. The influence of yield stress in mean pressure as a function of the contact: (a); for g=5 nm; (b) for g=10 nm.

Table 3.9. Mechanical properties of the materials considered to study the influence of Young's Modulus, *E*.

E (GPa)	ν	σ_y (GPa)
600		
400	0.42	5
200		

Table 3.9 summarizes the material characteristics considered to study the influence of the Young's Modulus. Three different values of Young's Modulus are analysed. The influence of the Young's Modulus on the mean pressure evolution is shown in Figure 3.26. It's observed that the mean pressure increases as the increasing of *E*. Besides, the transition from elastic to plastic behaviour occurs early for the highest *E*. Additionally, for the higher values of *E*, 400 GPa and 600 GPa, the mean pressure at yield inception is similar.

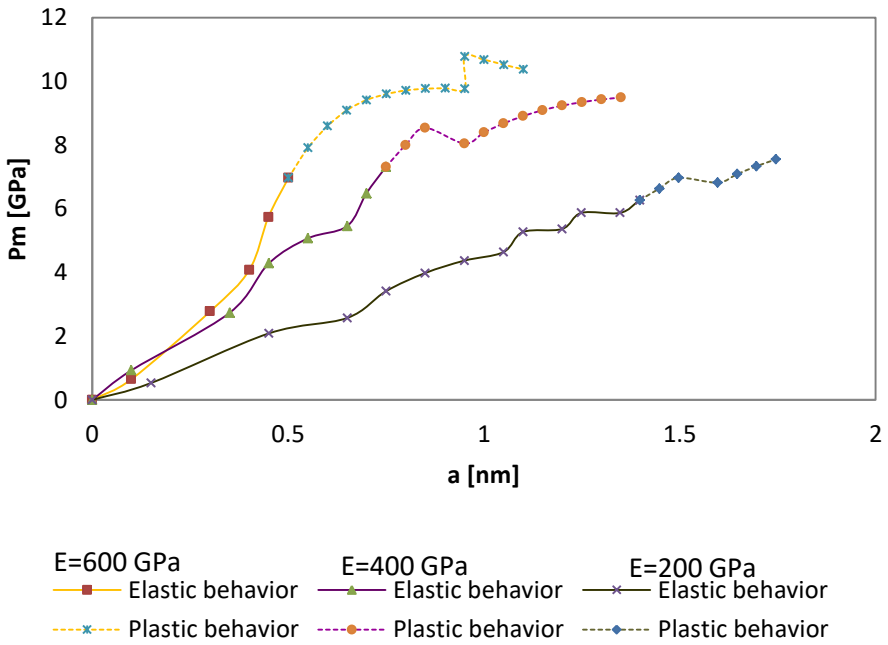

Figure 3.26. Mean pressure evolution as a function of the contact radius for g=10 nm and σ_y=5 GPa.

Table 3.10. Mechanical properties of the materials used to study the importance of Poisson's ratio, ν, in the material response.

E (GPa)	ν	σ_y (GPa)
60	0.42 0.3 0.2	1

Table 3.10 introduces different values attributed to ν, E and σ_y to the results exposed in this section for the Poisson's ratio influence. Figure 3.27 highlights that the highest Poisson's ratio requires a larger value of mean pressure in a transition from elastic to plastic behaviour. It's also visible that, for the same value of ν, the transition from elastic behaviour to plastic occurs for higher values of contact radius, while for the smaller values of υ it occurs with a smaller contact.

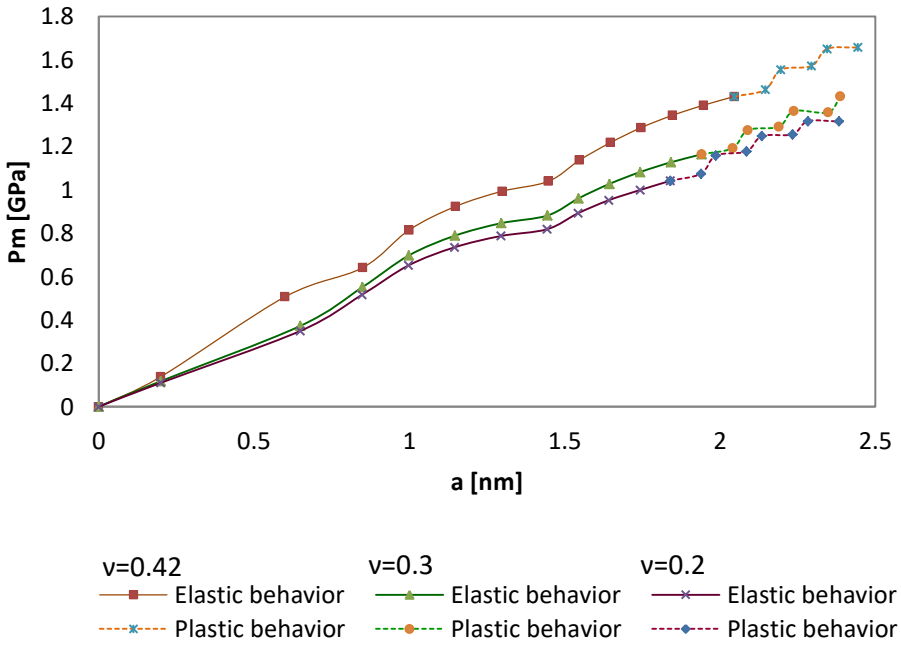

Figure 3.27. Mean pressure distribution as a function of the contact, a, for different values of ν.

3.7.3. Results and Discussion

For the 3D simulation results presented above, the values for the contact radius a were obtained manually, measuring the distance between nodes. Due to the coarse mesh the values aren't always as precise as it should be, creating an uneven evolution. Even so, the results were validated by literature (Liu & Proudhon, 2014) being considered valid.

Figure 3.28 shows the contact pressure distribution in the elastic regime for a simulation with $g = 5\,\text{nm}$, $E = 60$ GPa, $\sigma_y = 1$ GPa and $\nu = 0.42$. The maximum value for the contact pressure is always registered at the centre of the asperity. Since the material is assumed isotropic and the asperity geometry is axisymmetric, it is expected to obtain an axisymmetric distribution of the contact pressure. However, the obtained contact pressure presents a slight deviation, as shown in Figure 3.28. Even though a refined finite element mesh was used (see Figure 3.5), the square shape distribution of the finite elements affects the contact pressure distribution. Since the results obtained were corroborated by literature (Liu & Proudhon, 2014), this is seen as an effect with no consequences for the veracity of the results.

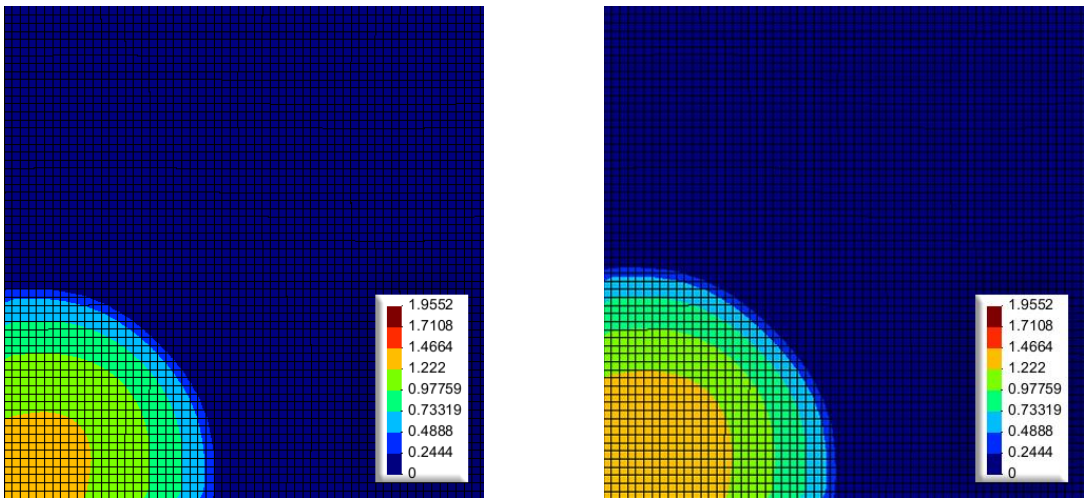

(a) (b)

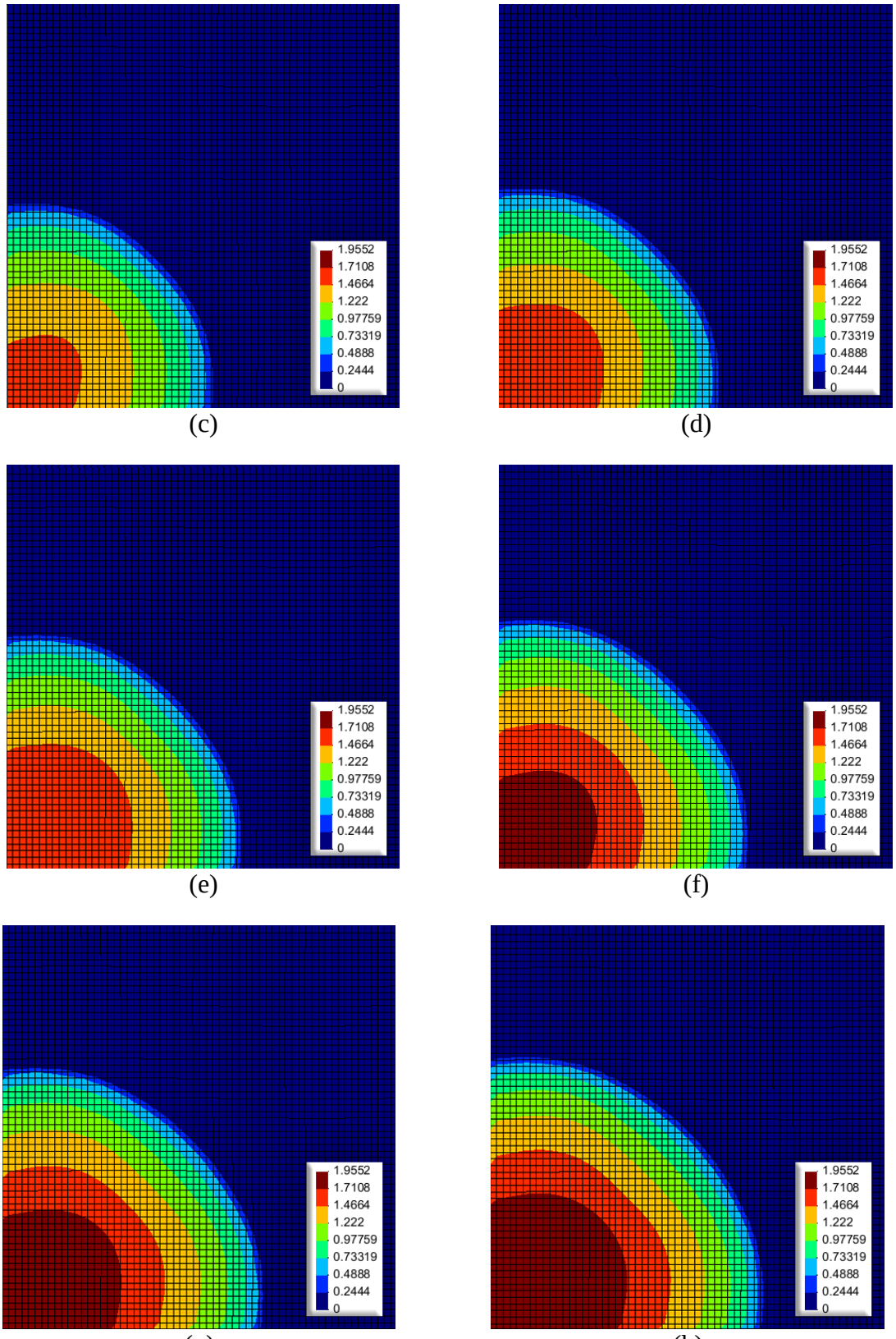

Figure 3.28. Top view of the asperity's tip showing the contact pressure distribution for a simulation in elastic regime for an interference of: (a) 0.038 nm; (b) 0.046 nm; (c) 0.053 nm; (d) 0.061 nm; (e) 0.068 nm; (f) 0.076 nm; (g) 0.083 nm; (h) 0.091nm .

It's an indisputable fact that the real contact area is much smaller than the apparent area, as explained in section 2. Figure 3.29 presents the ratio between the effective contact area, A_r, (red zone in Figure 3.10 (a) and Figure 3.22 (a)), and the apparent area, A_0, as a function of the real contact area. In both finite element models, it's observed that the real contact area is significantly smaller than an apparent area and the increase of the contact area is represented by a linear relation. This linear trend was previously observed in the studies of Greenwood & Williamson, 1966 and Yastrebov et al., 2011.

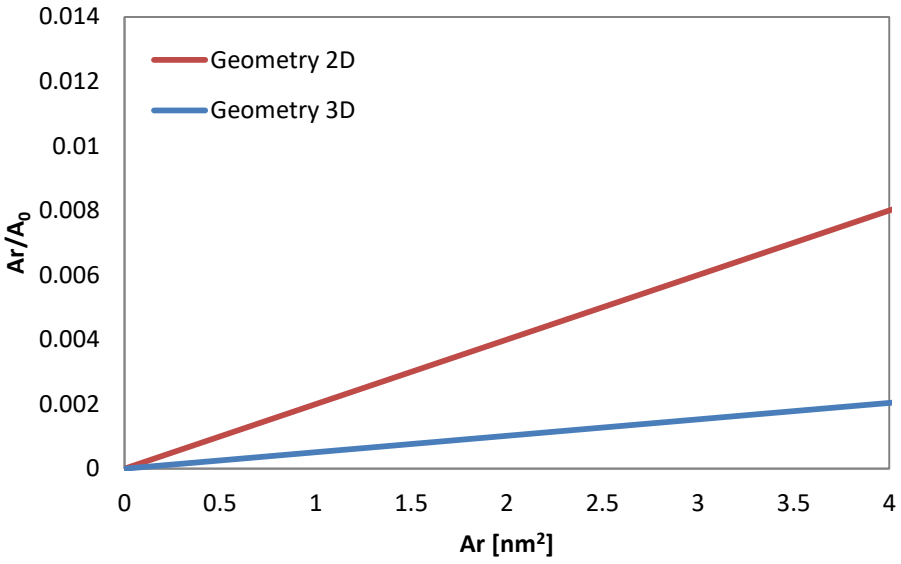

Figure 3.29. Ratio between effective contact area (A_r) and apparent contact area (A_0) as a function of effective contact area for 2D and 3D geometries.

Figure 3.30 shows the evolution of the pressure at the centre of the asperity's tip (maximum value) as a function of the ratio between the force applied and the apparent area. It's observed that the effective pressure in the asperity is always higher than the mean pressure. Besides, independently of the geometry, the maximum value of σ_z stabilizes for similar values. However, for small values of σ_y the pressure stabilizes earlier.

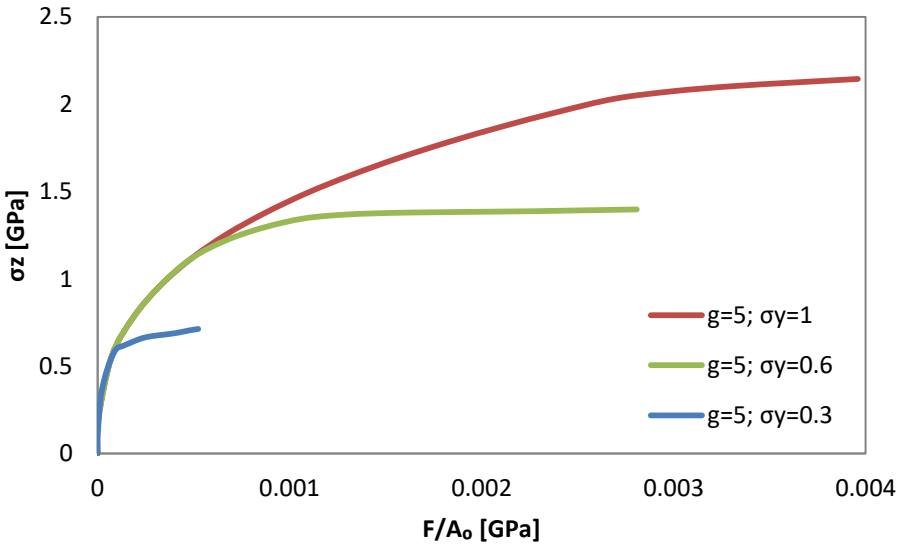

(a)

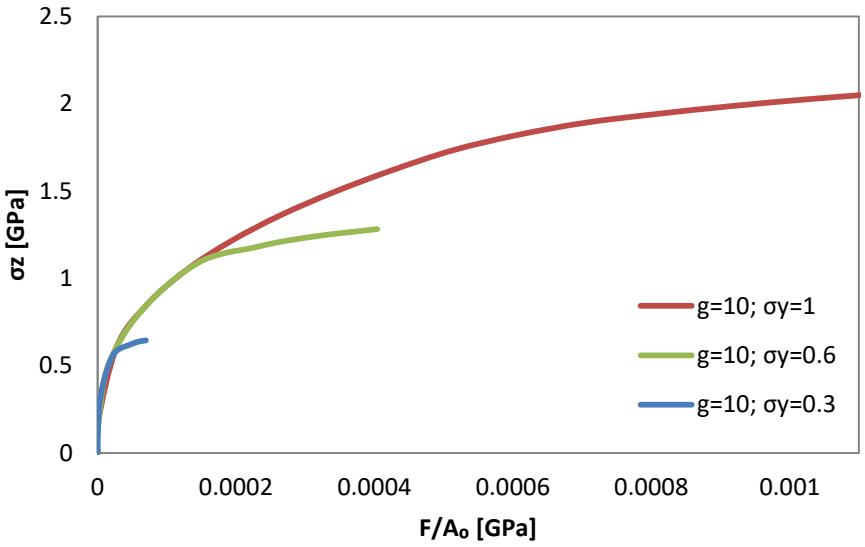

(b)

Figure 3.30. Distribution of the maximum contact pressure as a function of the mean pressure for different values of σ_y: (a) For g=5 nm; (b) for g=10 nm.

4. CONCLUSIONS

This study presents the finite element simulation of frictionless contact between a deformable sinusoidal asperity and a rigid flat surface. Both two- and three-dimensional models are developed to study the effects of geometrical and material parameters. Different geometries and material parameters were used, namely the height of the asperity's tip, the Young's modulus, the Poisson's ratio and the yield stress, which were selected based on studies carried out by other authors. The materials are considered elastic and plastic isotropic (von Mises), with a perfectly plastic behaviour. The evolution of the yield surface was described by Voce law. The in-house finite element code DD3IMP was used to perform all the simulations.

Regarding the 2D simulation results, contact can be approximately characterized by two parameters: ψ, which plays a role of a plasticity index (equation (3.11)), and α, (equation (3.10)) which can be regarded as a loading parameter. It can be established, about the material, that:

- When $\psi < 0.265$, the asperity remains in the elastic regime until the surface reaches complete contact ($\alpha = 0.5$);
- For $0.265 < \psi < 1.5$ and $\psi\alpha > 0.1$ the asperity will deform plastically but always within the elastic-plastic regime, up to full contact, and never reaching full plasticity;
- Within the elastic-plastic regime, $0.265 < \psi < 1.5$, the mean asperity contact pressure initially rises with α, till it reaches the maximum at the point when neighbouring asperities begin to interact, falling right after;
- For $\psi > 2$ the normalized mean pressure, for the same geometry, reaches a plateau for $\alpha = 0.2$, independently of the material properties (E/σ_y); for $\alpha > 0.3$ the mean asperity rises rapidly as $\alpha \to 0.5$ due to the beginning of the interaction of the plastic zones, under neighbouring asperities.

Concerning to the geometry, it is observed that for a geometry with a higher tip, is associated with a higher value of average mean pressure, reaching the same contact radius. The tips with $g = 1$ nm could never reach full plasticity. The Hertz theory for two cylinders with parallel axis provides an unsatisfactory solution for the evolution of the contact pressure distribution in comparison with the numerical simulations. Therefore, it's not possible to predict the pressure distribution in the contact between a sinusoidal and a flat surface, with the characteristics presented in this study.

In 3D simulations, the transition from elastic deformation to plastic deformation is smooth and continuous, being difficult to define accurately. For small plastic deformation it's observed the same trend that was under the pure elastic deformation. The height of the asperity's tip, Young's modulus and yield stress presents a large influence on the contact radius at yield inception, while the Poisson's ratio has weak influence on it. The average mean pressure strongly depends on the yield stress at the transition between elastic and plastic behaviours. Young's modulus and Poisson's ratio show a weak influence on the mean pressure at the yield inception and the height of the geometry's tip show no influence at all. The maximum pressure, measured at the centre of the asperity, represented as function average mean pressure for the apparent area, indicates similar values for g=5 nm and g=10 nm, stabilizing when material reaches the plastic regime, although the maximum pressure stabilizes for small values of the mean pressure when the asperity's tip is higher.

At yield inception, the contact radius is much larger for 2D model than in 3D models, as well as the contact area. In both models it is verified that when the tip of the asperity is higher, the material reaches the plastic behaviour earlier, for a small interference and a small contact radius. This phenomenon occurs due to the contact area being smaller. While the low geometry offers a larger contact area, a larger force is needed to reach plasticity.

REFERENCES

Archard, J. F. (1957). Elastic Deformation and the Laws of Friction. *Proceedings of the Royal Society of London. Series A. Mathematical and Physical Sciences*, *243*(1233), 190 LP-205. Retrieved from http://rspa.royalsocietypublishing.org/content/243/1233/190.abstract

Bobji, M. S., & Biswas, S. K. (1998). Estimation of hardness by nanoindentation of rough surfaces. *Journal of Materials Research*, *13.11*, 3227–3233.

Bowden, F. P., & Leben, L. (1939). The Nature of Sliding and the Analysis of Friction. *Proceedings of the Royal Society of London. Series A. Mathematical and Physical Sciences*, *169*(938), 371 LP-391. Retrieved from http://rspa.royalsocietypublishing.org/content/169/938/371.abstract

Bucher, F., Knothe, K., & Theiler, A. (2002). Normal and tangential contact problem of surfaces with measured roughness. *Wear*, *253*(1), 204–218. http://doi.org/10.1016/S0043-1648(02)00102-3

Chang, W. R., Etsion, I., & Bogy, D. B. (1987). An Elastic-Plastic Model for the Contact of Rough Surfaces. *Journal of Tribology*, *109*(2), 257–263. Retrieved from http://dx.doi.org/10.1115/1.3261348

Ciavarella, M., Demelio, G., Barber, J. R., & Jang, Y. H. (2000). Linear elastic contact of the Weierstrass profile. *Proceedings of the Royal Society of London. Series A: Mathematical, Physical and Engineering Sciences*, *456*(1994), 387 LP-405. Retrieved from http://rspa.royalsocietypublishing.org/content/456/1994/387.abstract

Dundurs, J., Tsai, K. C., & Keer, L. M. (1973). Contact between elastic bodies with wavy surfaces. *Journal of Elasticity*, *3*(2), 109–115. http://doi.org/10.1007/BF00045817

Dupont, P. E. (1992). The Effect of Coulomb Friction on the Existence and Uniqueness of the Forward Dynamics Problem. *Proceedings 1992 IEEE International Conference on Robotics and Automation*, 1442–1447.

Feeny, B., Guran, A., Hinrichs, N., & Popp, K. (1998). A Historical Review on Dry Friction and Stick-Slip Phenomena. *Applied Mechanics Reviews*, *51*(5), 321–341. Retrieved from http://dx.doi.org/10.1115/1.3099008

Gadelmawla, E. S., Koura, M. M., Maksoud, T. M. A., Elewa, I. M., & Soliman, H. H. (2002). Roughness parameters. *Journal of Materials Processing Technology*, *123*(1), 133–145. http://doi.org/10.1016/S0924-0136(02)00060-2

Gao, Y. F., Bower, A. F., Kim, K.-S., Lev, L., & Cheng, Y. T. (2006). The behavior of an elastic–perfectly plastic sinusoidal surface under contact loading. *Wear*, *261*(2), 145–154. http://doi.org/10.1016/j.wear.2005.09.016

Greenwood, JA and Tripp, J. (1970). The contact of two nominally flat rough surfaces. *Proceedings of the Institution of Mechanical Engineers*, *185*(1), 625–633.

Greenwood, J. A., & Tripp, J. H. (1967). The Elastic Contact of Rough Spheres. *Journal of Applied Mechanics*, *34*(1), 153–159. Retrieved from http://dx.doi.org/10.1115/1.3607616

Greenwood, J. A., & Williamson, J. B. P. (1966). Contact of Nominally Flat Surfaces. *Proceedings of the Royal Society of London A: Mathematical, Physical and Engineering Sciences*, *295*(1442), 300–319. http://doi.org/10.1098/rspa.1966.0242

Hol, J., Meinders, V. T., de Rooij, M. B., & van den Boogaard, A. H. (2015). Multi-scale friction modeling for sheet metal forming: The boundary lubrication regime. *Tribology International*, *81*, 112–128. http://doi.org/10.1016/j.triboint.2014.07.015

Hughes, T. J. R. (1980). Generalization of selective integration procedures to anisotropic and nonlinear media. *International Journal for Numerical Methods in Engineering*, *15*(9), 1413–1418. http://doi.org/10.1002/nme.1620150914

Hutchings, I. M. (2016). Leonardo da Vinci's studies of friction. *Wear*, *360*, 51–66. http://doi.org/10.1016/j.wear.2016.04.019

Johnson, K. L. (1987). *Contact Mechanics*.

Liu, M., & Proudhon, H. (2014). Finite element analysis of frictionless contact between a sinusoidal asperity and a rigid plane: Elastic and initially plastic deformations. *Mechanics of Materials*, *77*, 125–141. http://doi.org/10.1016/j.mechmat.2014.06.009

Majumdar, A., & Bhushan, B. (1990). Role of Fractal Geometry in Roughness Characterization and Contact Mechanics of Surfaces. *Journal of Tribology*, *112*(2), 205–216. Retrieved from http://dx.doi.org/10.1115/1.2920243

Mandelbrot, B. B., & Pignoni, R. (1983). *The fractal geometry of nature*.

Menezes, L. F., & Teodosiu, C. (2000). Three-dimensional numerical simulation of the deep-drawing process using solid finite elements. *Journal of Materials Processing*

Technology, *97*(1), 100–106. http://doi.org/10.1016/S0924-0136(99)00345-3

Mihailidis, A., Bakolas, V., & Drivakos, N. (2001). Subsurface stress field of a dry line contact. *Wear*, *249*(7), 546–556. http://doi.org/10.1016/S0043-1648(01)00542-7

Neto, D. M., Oliveira, M. C., Menezes, L. F., & Alves, J. L. (2014). Applying Nagata patches to smooth discretized surfaces used in 3D frictional contact problems. *Computer Methods in Applied Mechanics and Engineering*, *271*, 296–320. http://doi.org/10.1016/j.cma.2013.12.008

Neto, D. M. S. (2014). *Numerical simulation of frictional contact problems using nagata patches in surface smoothing*. University of Coimbra.

Oliveira, M. C., Alves, J. L., Chaparro, B. M., & Menezes, L. F. (2007). Study on the influence of work-hardening modeling in springback prediction. *International Journal of Plasticity*, *23*(3), 516–543. http://doi.org/10.1016/j.ijplas.2006.07.003

Polonsky, I. A., & Keer, L. M. (1999). A numerical method for solving rough contact problems based on the multi-level multi-summation and conjugate gradient techniques. *Wear*, *231*(2), 206–219. http://doi.org/10.1016/S0043-1648(99)00113-1

Sayles, R. S. (1996). Basic principles of rough surface contact analysis using numerical methods. *Tribology International*, *29*(8), 639–650. http://doi.org/10.1016/0301-679X(96)00016-3

Silva, A., Ribeiro, C., Dias, J., & Sousa, L. (2004). *Desenho Técnico Moderno* (11ª). LIDEL.

Yastrebov, V. A., Durand, J., Proudhon, H., & Cailletaud, G. (2011). Rough surface contact analysis by means of the Finite Element Method and of a new reduced model. *Comptes Rendus Mécanique*, *339*(7–8), 473–490. http://doi.org/10.1016/j.crme.2011.05.006